

Natural off-stoichiometry causes carrier doping in half-Heusler filled tetrahedral structures

Yonggang G. Yu,^{*} Xiuwen Zhang, and Alex Zunger[†]*University of Colorado Boulder, Renewable and Sustainable Energy Institute, Boulder, Colorado 80309, USA*

(Received 16 August 2016; published 3 February 2017)

The half-Heusler filled tetrahedral structures (FTSs) are zinc-blende-like compounds, where an additional atom is filling its previously empty interstitial site. The FTSs having 18 valence electrons per formula unit are an emerging family of functional materials, whose intrinsic doping trends underlying a wide range of electronic functionalities are yet to be understood. Interestingly, even pristine compounds without any attempt at impurity/chemical doping exhibit intriguing trends in the free carriers they exhibit. Applying the first principles theory of doping to a few prototype compounds in the $A^{\text{IV}}B^{\text{X}}C^{\text{IV}}$ and $A^{\text{IV}}B^{\text{IX}}C^{\text{V}}$ groups, we describe the key ingredients controlling the materials' propensity for both intrinsic and extrinsic doping: (a) The spontaneous deviations from 1:1:1 stoichiometry reflect predictable thermodynamic stability of specific *competing phases*. (b) Bulk ABC compounds containing $3d$ elements in the B position (ZrNiSn and ZrCoSb) are predicted to be naturally $3d$ rich. The $B = 3d$ interstitials are the prevailing shallow donors, whereas the potential acceptors (e.g., Zr vacancy and Sn-on-Zr antisite) are ineffective electron killers, resulting in an overall uncompensated n -type character, even without any chemical doping. In these materials, the band edges are "natural impurity bands" due to non-Daltonian off-stoichiometry, such as B interstitials, not intrinsic bulk controlled states as in a perfect crystal. (c) Bulk ABC compounds containing $5d$ elements in the B position (ZrPtSn, ZrIrSb, and TaIrGe) are predicted to be naturally C rich and A poor. This promotes the hole-producing C -on- A antisite defects rather than B -interstitial donors. The resultant p -type character (without chemical doping) therein is "latent" for $C = \text{Sn}$ and Sb ; however, as the C -on- A hole-producing acceptors are rather deep and p typeness is manifest only at high temperature or via impurity doping. In contrast, in TaIrGe ($B = \text{Ir}$, $5d$), the prevailing hole-producing Ge-on-Ta antisite (C -on- A) is shallow, making it a real p -type compound. This general physical picture establishes the basic trends of carriers in this group of materials.

DOI: [10.1103/PhysRevB.95.085201](https://doi.org/10.1103/PhysRevB.95.085201)

I. INTRODUCTION: THE FAMILIES OF HALF-HEUSLER FILLED-TETRAHEDRAL STRUCTURE COMPOUNDS WITH 18 VALENCE ELECTRONS

Nature's most succinct ternary structures belong to the 1:1:1 equiatomic ABC compounds [1–3]. They encompass two main families: (i) the eight valence-electron (octet) family [3–9] containing the groups $A^{\text{I}}B^{\text{II}}C^{\text{V}}$ (e.g., LiZnP), $A^{\text{I}}B^{\text{III}}C^{\text{IV}}$ (e.g., LiGaSi), $A^{\text{II}}B^{\text{II}}C^{\text{IV}}$ (e.g., MgSrSi), and $A^{\text{II}}B^{\text{III}}C^{\text{III}}$ (e.g., MgYGa) and (ii) the 18 valence-electron family [10–14] that appears in a few chemical groups, such as $A^{\text{III}}B^{\text{X}}C^{\text{V}}$ (e.g., ScPtSb), $A^{\text{IV}}B^{\text{X}}C^{\text{IV}}$ (e.g., ZrNiSn), $A^{\text{IV}}B^{\text{IX}}C^{\text{V}}$ (e.g., TiCoSb), and $A^{\text{V}}B^{\text{IX}}C^{\text{IV}}$ (e.g., TaIrGe [12–14]). These are "multifunctional materials" [11], due to their capacity to host a rich variety of $3d$, $4d$, and $5d$ transition metal elements and because of their appearance in numerous (over 40) crystal structure types, as summarized in Ref. [12], based on the Inorganic Crystal Structure Database (ICSD) [15]. The combination of structures and elements provides opportunities for tuning and designing electronic band structures, spin-orbit coupling effect, thermal and electrical conductivity, and optical transparency [10,11,14,16–19]. Some unique functionalities achievable in such compounds include thermoelectricity [20–22] (e.g., in TiNiSn and ZrCoSb), topological insulation (e.g., in ScPtBi [13]), transparent conductivity (e.g., in TaIrGe [14]),

Rashba spin splitting [23], magnetism [24,25], and superconductivity (e.g., YPtBi [26]).

The ABC families became recently a testing ground for theoretical material discovery by design approach [11,12,16–19,27,28], followed by experimental validation [13,14,29,30]. There are 483 element combinations of these 18 electron compounds listed in Ref. [13], of which 83 were previously synthesized [15] and 400 are plausible element combinations that were never reported ("missing compounds"). Recent theoretical predictions [13] applying the first principles materials-by-design approach [31–33] to the 483 possibilities showed that 54 of the 400 missing are predicted to be stable new compounds, 342 were predicted to be thermodynamically unstable, and four were too close to call. Synthesis of 17 of these predicted stable compounds was attempted; the structure determination agreed with predictions in all cases [13,14,30]. The four chemical groups involved in this paper are shown in Fig. 1, where previously known versus recently predicted and subsequently synthesized cases are indicated.

A central issue common to all newly introduced electronic materials dwells on whether carrier doping can be accomplished. This issue has only been explored experimentally for just a few filled tetrahedral structure (FTS) compounds, including ZrNiSn and TiCoSb [14,20,22,34–39]. The purpose of this paper is to understand the basic physical trends in self-doping (due to natural off-stoichiometry), as well as some impurity doping in this family of electronic materials. Section II will highlight the main issues and summarize the key insights expanded upon in the remainder of this paper.

^{*}Present address: Cooperative Institute for Research in Environmental Sciences, University of Colorado, Boulder, Colorado 80309, USA; yonggang.yu@colorado.edu

[†]alex.zunger@colorado.edu

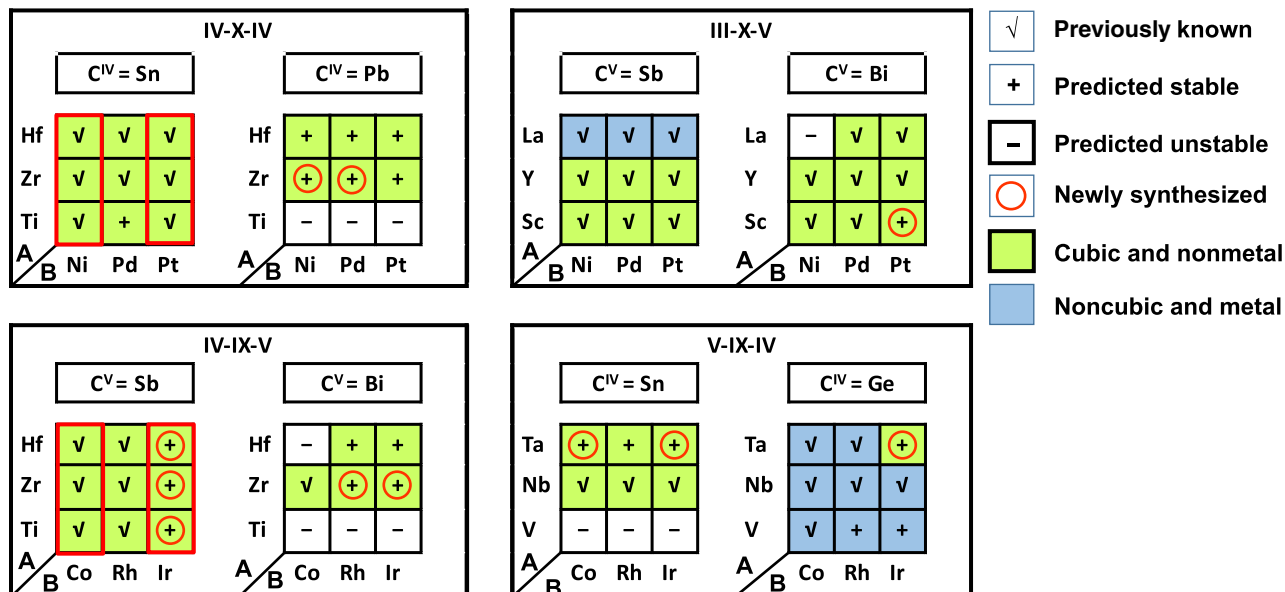


FIG. 1. Four of the existing chemical groups of the 18 electron ABC ternary materials containing 72 possible compounds, of which 40 are previously synthesized known compounds (denoted by \checkmark sign). Of the 32 unreported, 21 are now predicted stable (denoted by $+$ sign), and 11 are predicted unstable (denoted by $-$ sign). Of the 21 newly predicted compounds, 11 were recently attempted and successfully synthesized in the predicted structure [13] (shown in red circles). The ternary compounds with cubic space group $F\bar{4}3m$ are nonmetals (shaded green), whereas the noncubic compounds are metal (shaded blue). Their band gaps from hybrid functional calculations are shown in Appendix. Red circles denote recently synthesized compounds [13], and red rectangles denote a subset of $A^{\text{IV}}BC$ cubic semiconducting compounds whose carrier doping properties may be representative to this family.

II. KEY ISSUES PERTAINING TO INTRODUCTION OF CARRIERS IN FILLED TETRAHEDRAL HALF-HEUSLER COMPOUNDS

Two approaches are viable for introduction of free carriers into half-Heusler compounds: external chemical (impurity) doping and natural self-doping, existing in as-grown compounds due to natural off-stoichiometry (intrinsic). Carrier types in ABC compounds due to impurity doping are often explained by textbook element substitution rules: substituting a host atom in solid by an impurity atom with higher (lower) valence induces n -type (p -type) conductivity. For example, Nb or Ta doping on the Zr-site, and Sb or Bi doping on the Sn-site in $ZrNiSn$ result in n -type carriers, while Sc-doped $ZrNiSn$ (on Zr-site) [40], Sn-doped $ZrCoSb$ (on Sb-site) [41], and Fe-doped $TiCoSb$ (Co site) [42] are p type. In contrast, natural carrier generation in pristine samples continue to bring in surprises on carrier types, as well as carrier dependence on temperature, as new experimental results emerge. We will discuss intrinsic doping in Secs. IV A–IV C, illustrate impurity doping in Sec. IV D, and articulate our proposed conceptual framework for doping in Sec. V. Our stoichiometry and defect computation and physical analysis (Secs. III and IV) lead to the following key perspectives on doping ABC compounds, which interpret a range of experiment and provide insights into the problem.

A. Natural off-stoichiometry is generally reflected by compound thermodynamics and controls electrical behavior

Unlike Daltonian compounds with strict stoichiometry, half-Heusler compounds (Fig. 2) are prone to chemical off-stoichiometry, which strongly influences their carrier

and defect properties. A number of such compositions were empirically observed in the FTS phase (in the $MgAgAs$ structure) in the past, e.g., $ZrNi_{1+x}Sn_{1-y}$ ($x = 6\%$, $y = 0.8\%$) [43], $ZrNi_{1+x}Sn$ ($x = 0-10\%$) [44], $HfNi_{1+x}Sn$ ($x = 0-25\%$) [44], and $Ti_{1+x}Ni_{1+y}Sn$ ($x = 4\%$, $y = 3\%$) [36]. The theoretical question posed here is what causes off-stoichiometry and how it affects carrier doping.

While some of the off-stoichiometry may be enhanced or diminished by control of metastable condition or nonequilibrium (e.g., over or under saturation of reactants), the basic trends of a given sublattice being persistently off-stoichiometric in a particular direction is thermodynamically predictable. We observed an interesting phenomenon from calculations—when the B atom is a $3d$ transition metal element (e.g., $ZrNiSn$ and $ZrCoSb$), the off-stoichiometry is in the direction of B excess, but when B is a $5d$ element (e.g., $HfPtSn$ and $TiIrSb$) the off-stoichiometry is C rich and A poor. Such off-stoichiometry is a direct consequence of the thermodynamic competition between the host and its competing phases (discussed in Sec. III B). Off-stoichiometry induces preferential defects; the latter then creates electric carriers if they can ionize at finite temperature, as will be discussed in Sec. IV.

B. The thermodynamic preference for specific deviations from perfect stoichiometry controls specific intrinsic defect types

An immediate outcome of the understanding of the origin of natural off-stoichiometry is that one can predict theoretically from thermodynamic stability versus chemical potentials (e.g., Fig. 3) the likely charge neutral intrinsic defects that will abound. We will show that because the stability domains of $ANiSn$ and $ACoSB$ ($A = Ti, Zr, \text{ and } Hf$) lie at the upper

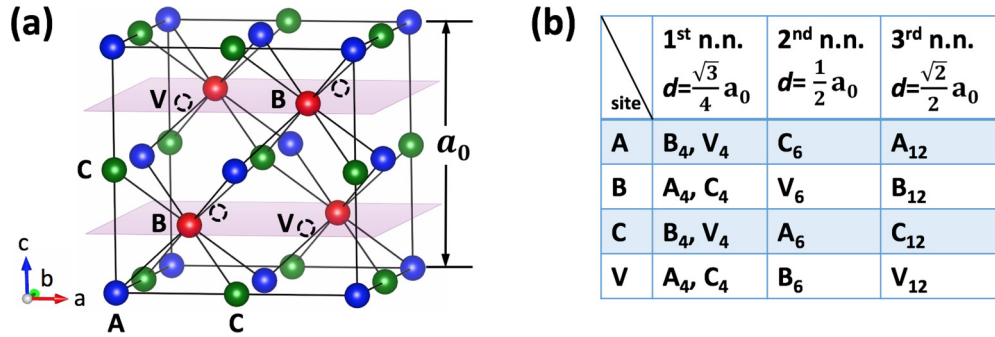


FIG. 2. (a) Illustration of the four crystallographic sites in cubic FTS with T_d symmetry (A site, B site, C site, and vacant site). (b) Atomic identity and bond distances of the first three nearest neighbor (n.n.) coordination shells around each site.

half of the full triangle frame (Fig. 3), these compounds are naturally B element rich ($B = \text{Ni}$ or $B = \text{Co}$). This implies the possibility of B interstitials and B antisite defects (B -on- A or B -on- C) and the scarcity of B vacancies. On the other hand, we will show that the stability domain of APtSn and AlrSb ($A = \text{Ti}, \text{Zr},$ and Hf) are mainly constrained towards the hypotenuse side of the full chemical potential triangle frame, indicating a C -rich condition ($C = \text{Sn}$ or $C = \text{Sb}$) and lack of a B -rich condition. This implies the possibility of C -on- A , C -on- B , or C interstitial defects and the lack of B interstitials in these groups. This is discussed in Secs. III A and B and Figs. 2–3.

C. Crystallographic factors, such as conservation of coordination numbers (CNs), contribute to the selectivity of specific intrinsic defect structures

Our total energy studies substantiate another key controlling factor: The role of conservation or violation of the original CN. In the ABC cubic half-Heusler FTS compounds, the A and C sites are fourfold coordinated, whereas the B site is eightfold coordinated (Fig. 2). We find that if an intrinsic defect conserves the original CN (as in A -on- C and C -on- A antisite defects with $\text{CN} = 4$), its formation energy is rather low, so the defect would be likely to form. If, on the other hand, the defect does not conserve the original CN (as in B -on- A , B -on- C , as well as A -on- B and C -on- B antisite defects), these defects would be energetically less likely. This simple rule is discussed in Sec. III C and Fig. 2 and confirmed by quantitative defect formation energy calculations, and by charge neutral defect concentration calculation from Fig. 4.

D. Certain ABC compounds cannot be impurity doped, while others can, depending on the thermodynamic driving force to spontaneously form opposing defects

How the defect system responds to external impurity doping is critical to the intended carrier generation. In general [45], intrinsic “killer defects” can appear spontaneously and negate the intended carrier doping. For instance, deliberate introduction of electron via donor doping tends to shift the Fermi energy towards the conduction band, but at the same time, this will lower the formation energy required to create intrinsic “electron killers” (acceptors), such as cation vacancies. We will show that there are no such natural killer defects for n -type doping in ZrNiSn and ZrCoSb , but in contrast, the p -type doping in ZrIrSb is opposed by Sb-on-Zr

(+1) defect, rendering this compound only weakly p type. This explains why certain deliberate chemical doping needs to overcome the natural tendency of the host compound to develop compensating defects. This is discussed in Sec. IV D.

E. The band gap anomaly in pristine $A^{\text{IV}}B^{\text{X}}C^{\text{IV}}$ compounds and its origin

For many FTS compounds, the observed band gap tends to be significantly *smaller* than what can be inferred from perfect single crystals (when they exist) or from those predicted by the density functional calculations, a surprising result given that density functional theory (DFT) generally *underestimates* band gaps relative to experiment [46]. For example, plain local density approximation (LDA) and generalized gradient approximation (GGA) predict for stoichiometric ZrNiSn a band gap at ~ 0.5 eV, yet a most recent experimental measurement by Schmitt *et al.* [47] gives a band gap of 0.13 eV, in agreement with early experimental value of ~ 0.18 eV of Aliev *et al.* [48]. While the anomalously small observed band gaps are beneficial to thermoelectric applications, understanding the origin of the anomaly has been controversial. Here, we briefly note the leading literature opinions and summarize the insights on this problem gained from our calculations:

1. A literature suggestion: Band gap reduction in ABC results from C -on- A atomic exchange (e.g., Sn-Zr exchange in ZrNiSn)

Aliev *et al.* [48] proposed on the basis of x-ray analysis an A - C exchange reaction producing a pair of antisite defects: A -on- C , as well as C -on- A (for example, a pair of Sn and Zr atom exchange in ZrNiSn). This idea offered a viable path to reconcile the smaller experimental band gap relative to expectations from stoichiometric DFT prediction, because the band gap reduction in ZrNiSn at a small Sn/Zr exchange ratio was indeed found from DFT band structure calculations [49,50]. However, recently, more accurate structure refinement from Xie *et al.* [43] observed no A - C exchange, which is consistent with DFT total energy calculations of Larson *et al.* [51], who showed that such exchange would be prohibitively costly in formation energy. Thus, this exchange reaction likely does not happen, so it cannot lead to gap reduction in practice. We will show in Sec. IV that, in general, by calculating simultaneously thermodynamic stability (formation enthalpy) of defects, as well as their (donor and acceptor) energy levels, we can establish (a) if a defect can exist in significant concentration

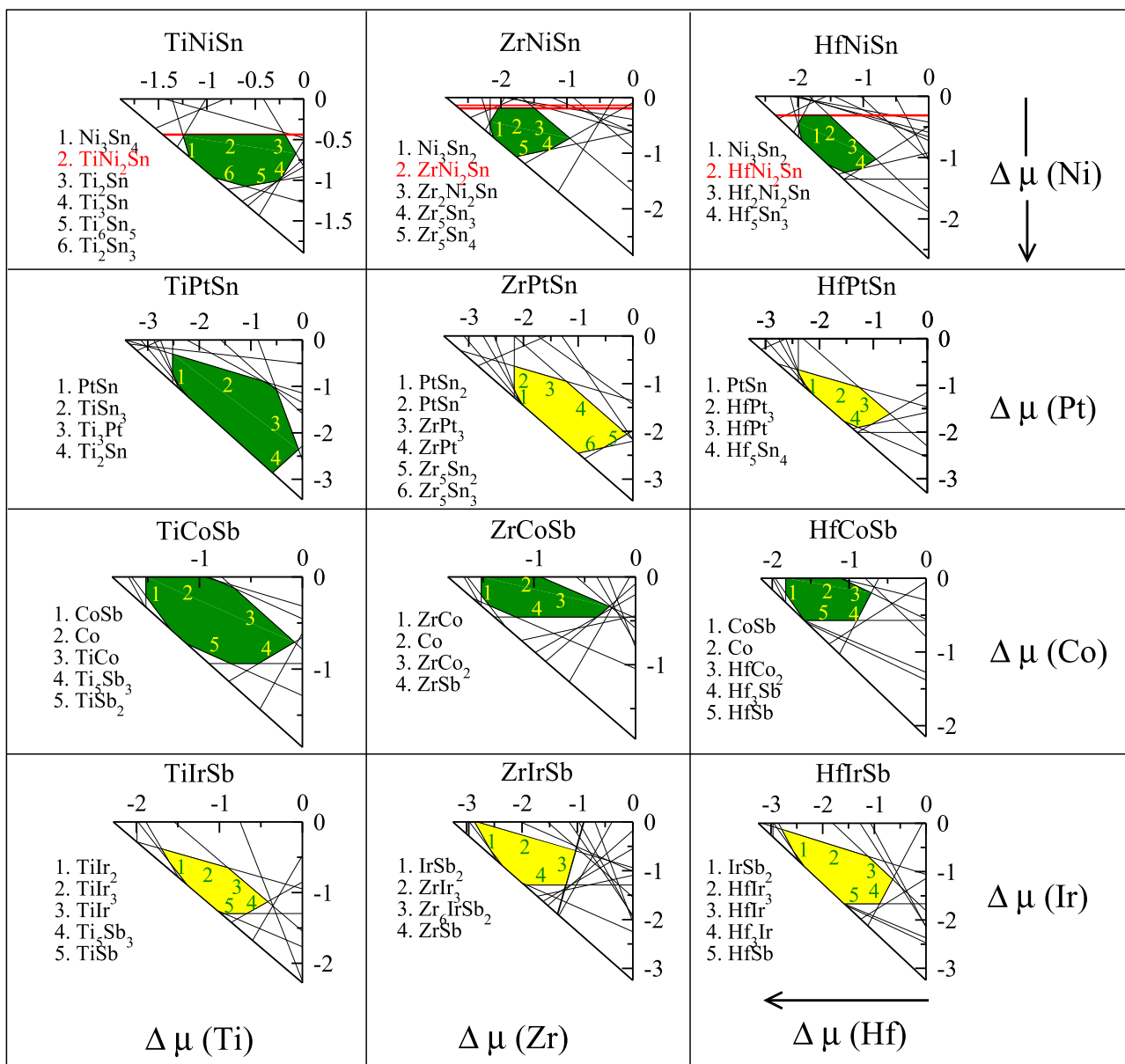


FIG. 3. The allowed chemical potential regions (green and yellow) in the $\Delta\mu_A$ versus $\Delta\mu_B$ plane of 12 cubic semiconducting $A^{IV}BC$ compounds, indicating also some of the phases competing with the stability of the ABC structure. A full list of competing phases is given in the Appendix. The green and yellow shadings serve as guide to the eye for B element rich and C element rich chemical conditions, respectively. The chemical stability fields of the $3d$ -containing $A^{IV}NiSn$ and $A^{IV}CoSb$ ($A^{IV} = Ti, Zr,$ and Hf) lie mainly at the upper half of the triangle axis frame, indicating B element rich conditions (Ni or Co rich), while the stability fields of the $5d$ -containing $A^{IV}PtSn$ and $A^{IV}IrSb$ are mainly constrained towards the hypotenuse side of the triangle axis frame, indicating C element rich (Sn or Sb rich). $TiPtSn$ has a relatively large chemical stability field, which contains both a B -rich and C -rich stability field regime, and we tentatively associate it with the green color group (B rich).

and (b) what is its electrical effect. If (a) is not satisfied, (b) is a moot point. This is the case for C -on- A atomic exchanges in FTS.

2. A literature suggestion: Band gap reduction in ABC could result from B atom Frenkel pair formation

The work from Larson *et al.* [51] and Romaka *et al.* [44] suggested that Ni Frenkel pairs in $ZrNiSn$ could reduce its

band gap because both calculations showed metallic states when a portion of Ni atoms (>25%) migrate from the host B sublattice to the vacant site. Our study shows that the thermodynamic energy cost tends to exclude its existence in optically significant concentrations, as shown in the Appendix. Again, calculations of the total energy (not just defect levels) of this sort act to validate or refute prior intuitive ideas.

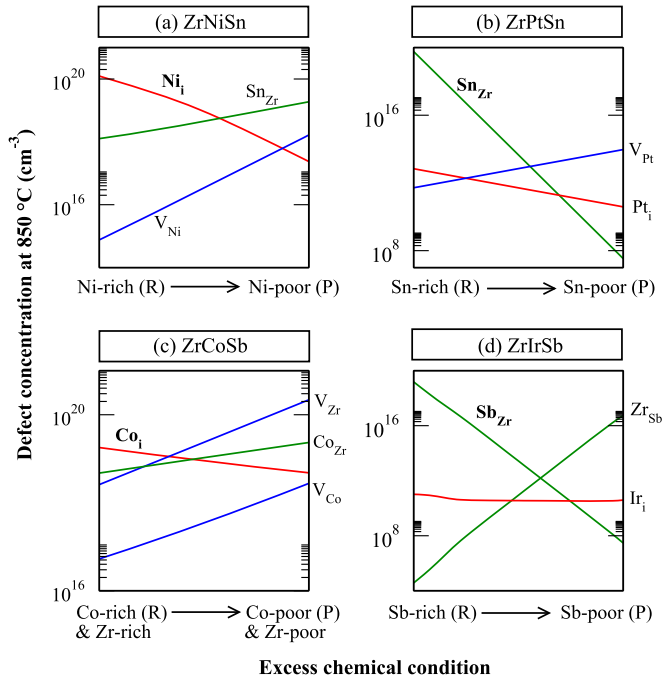


FIG. 4. The concentration of the dominant defects (each summed over all of its charged states) varying with the chemical growth condition along the line rich (R)-poor (P) in Fig. 9 at $T_g = 850$ °C. The red, blue, and green colors denote interstitial, vacancy, and antisite defects, respectively.

3. Calculations on a few members of the $A^{IV}B^XC^{IV}$ group show that the origin of gap reduction in a few members of the $A^{IV}B^XC^{IV}$ group is the formation of impurity band in the gap due to B interstitials

Specifically, we will show that Ni excess in off-stoichiometric ZrNiSn leads to an impurity band above the original (perfect crystal) valence band maximum (VBM), while at the same time, lowering the original conduction band due to the emergence of a “perturbed host state” (PHS) from the conduction band of the perfect crystal (see Lany and Zunger [52] and Kent and Zunger [53] for the discussion of the concept of PHS). Both effects, described in Sec. IV B, lead to a significant reduction of the band gap due to off-stoichiometry. The type of compounds that could show a high concentration of B interstitials is hinted by the existence of a stable full-Heusler analog AB_2C to the half-Heusler compound ABC in certain cases, such as $ZrNi_2Sn$ and $ZrNiSn$. This suggests mutual solubility at high temperatures (for details see Appendix), leading to Ni-Ni clustering, in agreement with Do *et al.* [54]. For high enough concentration of the B interstitial, there will be gap closure and a nonmetal to metal transition. This is discussed in Sec. IV B. The concept of excess Ni atoms accumulating at the interstitial sites in ZrNiSn is consistent with the photoemission experiment by Miyamoto *et al.* [55], showing two types of Ni sites in pure ZrNiSn samples: the host Ni site and the interstitial Ni site. That the excess Ni can introduce electronic in-gap states in density of states for ZrNiSn was simulated from DFT [51,54], with the observed low-band-gap, semiconductor electrical behavior of $ZrNi_{1+x}Sn$ ($x < 0.1$) [22,43,47,48,55,56]. We conclude that

in these materials, the band edges are “natural impurity bands” due to non-Daltonian off-stoichiometry, not intrinsic bulk controlled states as in a perfect crystal.

F. The origin of carriers in self-doped pure FTS compounds

The interesting aspect of off-stoichiometry in ABC compounds is that it introduces systematically and deterministically a particular type of carrier (electrons versus holes). In an attempt to explore novel thermoelectric materials, electrical properties of many half-Heusler compounds have been measured. The basic phenomenology noted is that n -type materials include ANiSn ($A = Ti, Zr, Hf$) and ACoSb ($A = Ti, Zr, Hf$), whereas p -type compounds include APtSn ($A = Zr$ and Hf), TaIrGe, ZrIrSb, YPtSb [57], $LnPdSb$ ($Ln = Y, Ho, Er, La, Gd$) [58], and $LnPdBi$ ($Ln = Nd, Y, Dy, Ho, Er, La, Gd$) [59].

The origin of n -type doping in the paramagnetic ZrNiSn case was speculated in a number of papers. It was suggested that a B -on- A antisite in ABC compounds would create free electrons. For example, the suggestion by Romaka *et al.* [56] assigned the Ni-on-Zr antisite defect as electron donors in ZrNiSn. Our calculation reveals that in ZrNiSn at any allowed chemical condition, the Ni-on-Zr defect formation energy is rather high (above 2 eV), so the concentration of this defect is significantly low (below 10^{14} cm^{-3}) and negligible in the system.

1. The origin of n -type carriers in undoped ABC compound with $B = 3d$ elements is ionized B atom interstitials

This explains the n -type behavior in ANiSn and ACoSb ($A = Ti, Zr, Hf$). This finding is at first surprising because it was generally assumed that a Ni interstitial with its closed shell d^{10} configuration would be a deep donor and not capable to explain the n -type behavior in normal samples (ZrNiSn). We will show that in ABC compounds with $B = 3d$ element, the B interstitial is not a deep donor but can be ionized, rendering the pure compound n type. Indeed, we find (see Fig. 5) that the spin exchange interaction in ionized Ni interstitial ($1+$) in ZrNiSn splits the d band into spin up (resonant in the valence band) and spin down near the conduction band minimum (CBM), with the latter spin level being effectively a shallow donor that contributes free electrons. In ZrCoSb, the ionized Co interstitial in $1+$ state is stable due to the effective d^8 configuration, where the ionized electronic state falls above the conduction band. This explains the n typeness due to $3d$ interstitials. Such ionization can also produce finite local magnetic moments at a dilute defect limit (Sec. IV B). The portion of ionized B interstitials strongly depends on the donor transition level relative to the host CBM, calculated by the Heyd-Scuseria-Ernzerhof (HSE) [60] exchange correlation. In ZrNiSn, the calculated carrier density lies in the range of 10^{18} to 10^{20} cm^{-3} and increases with temperature, while the calculated equilibrium Ni interstitial defect content can reach a maximum of 0.6% (see Sec. IV for details).

2. The origin of p -type carriers in undoped ABC compound with $B = 5d$ element is the C -on- A antisite defect

This explains the p -type behavior in TaIrGe, ZrIrSb, and APtSn ($A = Zr, Hf$). Previously, the contrast between n -type

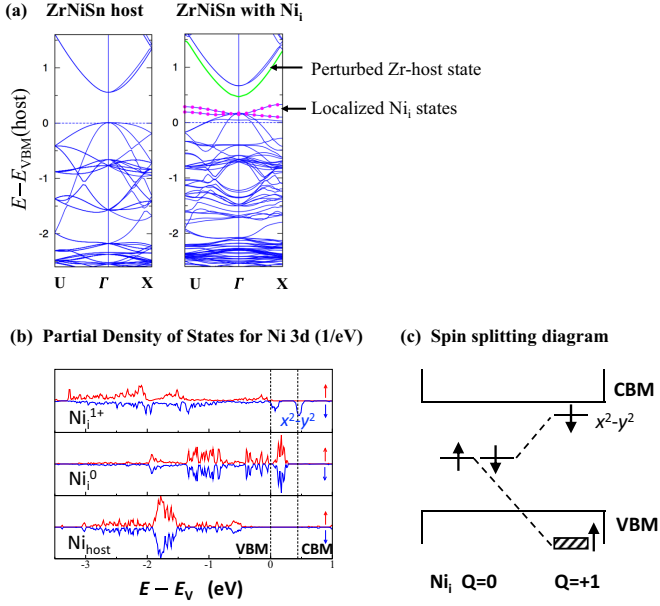


FIG. 5. (a) Electronic band structure of defect-free ZrNiSn supercell (48 atom) compared with the supercell containing one Ni_i impurity (49 atom) calculated by the HSE functional in a bcc-type unit cell: $U = (1/2, 1/2, 1/2)$ and $X = (1/2, 0, 0)$. (b) The projected partial density of states (PDOS) from Ni $3d$ states in a 49-atom supercell containing one Ni_i impurity in $1+$ and neutral charge state compared with PDOS in the defect-free supercell (48 atom). Red and blue denote opposite spin states. (c) A schematic illustration of eigenvalues for the spin-up and spin-down highest occupied molecular orbital (HOMO) states in a supercell containing one Ni_i^0 impurity ($Q = 0$), and the spin splitting scheme in the Ni_i^+ impurity state ($Q = +1$).

ZrNiSn and p -type ZrPtSn was unexplained, and stoichiometric disorder across the Zr and Sn sublattices was proposed assuming charge neutral states, which reduces the band gap but does not explain the origin of free holes therein [48,49]. We will elucidate the acceptor nature of the C -on- A antisite defect in this group of $B = 5d$ ABC compounds and quantify the charge compensation scenario in some of these compounds. Our results point to a different explanation: *the negatively charged C-on-A antisite defects form spontaneously and create holes in the ABC compounds with $B = 5d$ elements at favorable chemical conditions.*

The present paper will parse in sequence the specific ingredients that leads to conclusion of n -type (p -type) self-doping in filled tetrahedral half-Heusler compounds, propose a useful rule to help explain the doping trend in $B = 3d$ and $5d$ compounds, and present in detail our specific observations from this series of calculations.

III. RESULTS: INFERENCE FROM PRISTINE BULK ABC COMPOUNDS ON THEIR PROPENSITY TO FORM SPECIFIC INTRINSIC DEFECTS

A. The compounds selected here and their structures

Our material selection family begins with four prototype chemical groups: $A^{IV}B^XC^{IV}$, $A^{IV}B^{IX}C^V$, $A^{III}B^XC^V$, and $A^VB^{IX}C^{IV}$ containing 72 compounds (Fig. 1). Of these, a total of 61 are predicted to be thermodynamically stable (combining

40 previously made with 21 previously missing but predicted stable). Of the 61 stable compounds, 50 are cubic nonmetals (shaded in green in Fig. 1), and the remaining 11 are noncubic structures and are metals (shaded in blue) [13]. Only the 50 nonmetals are candidates for meaningful defect calculations. The $A^VB^{IX}C^{IV}$ group in Fig. 1 has been eliminated because of a small number of semiconducting compounds. We, likewise, avoid the semimetallic $A^{III}B^XC^V$ group ($C = Sb$ and Bi), where a majority of ternaries show band gaps below 0.5 eV (HSE results in the Appendix). Among the other semiconductor groups of ABC , which are more suitable for defect calculations, we focus on the $ANiSn$, $APtSn$, $ACoSb$, and $AIrSb$ series ($A = Ti, Zr$, and Hf) forming a natural set with both A -atom and B -atom variations. The similarity between Ti, Zr , and Hf elements in their chemical bonds and in their atomic radii (Ti : 2.0 Å and Zr and Hf : 2.16 Å) suggests it is suitable to choose $A = Zr$ in the four series of compounds for an illustrative study. This leads to our final choice of four compounds for a carrier doping study: ZrNiSn, ZrCoSb, ZrPtSn, and ZrIrSb, with the first three being previously made compounds and the last one being a recently predicted and newly synthesized compound. Table I gives the calculated lattice constants and band gaps of the bulk compounds, which is also seen from band structure calculations in the Appendix.

The *cubic* half-Heusler compounds are all semiconductors (see Table I) and exist in the FTS with space group $F\bar{4}3m$ [3–6] (Fig. 2). In the ground state structure, the B element is the group-IX element (Co, Rh, and Ir) or group-X element (Ni, Pd, and Pt) located at the eightfold site, while the A and C elements occupy the fcc sublattice, each having four B and four vacant sites as nearest neighbors (see the first three coordination shells around each site in Fig. 2). We find that swapping the two elements between the eightfold (B -site) and fourfold site (A or C site) in the ground state structure is energetically unfavorable, costing on average 0.7 eV/f.u. (see Appendix).

TABLE I. Fundamental electronic band gaps of the $A^{IV}NiSn$, $A^{IV}PtSn$, $A^{IV}CoSb$, and $A^{IV}IrSb$ groups ($A = Ti, Zr$, and Hf) half-Heusler compounds using hybrid functional calculations (HSE) [60,70,71]. All HSE fundamental gaps are of the $\Gamma - X$ indirect character, except $HfIrSb$, which has a direct gap (see band structures in Appendix). The lattice constant was relaxed by the GGA + U method.

| Compound | a_0 (Å) | E_g (HSE) (eV) | Experimental carrier types |
|----------|-----------|------------------|----------------------------|
| TiNiSn | 5.95 | 0.60 | n [37,43,65,72] |
| ZrNiSn | 6.19 | 0.55 | n [43] |
| HfNiSn | 6.16 | 0.45 | n [22] |
| TiPtSn | 6.23 | 1.31 | n/p [69] |
| ZrPtSn | 6.44 | 1.28 | p [69] |
| HfPtSn | 6.41 | 1.20 | p [69] |
| TiCoSb | 5.90 | 1.42 | n [34,38] |
| ZrCoSb | 6.13 | 1.49 | n [34] |
| HfCoSb | 6.10 | 1.41 | n [34] |
| TiIrSb | 6.38 | 1.70 | |
| ZrIrSb | 6.35 | 2.06 | p [13] |
| HfIrSb | 6.18 | 1.57 | |

B. The chemical stability field reveals tendencies towards off-stoichiometry and identifies the leading charge neutral defects

The formation of ABC ternary under a given set of chemical potential condition with $\Delta\mu_{A,B,C} < 0$ requires that $\Delta\mu_A + \Delta\mu_B + \Delta\mu_C = \Delta H(ABC)$, where $\Delta H(ABC)$ is the compound formation energy. Projection of this equation onto the $\{\Delta\mu_A, \Delta\mu_B\}$ plane leads to a chemical potential triangle frame $\Delta\mu_A + \Delta\mu_B > \Delta H(ABC)$, with $\Delta\mu_{A,B} < 0$. Further constraints to the triangle arise from the ABC ternary being stable against decomposition or converting into its competing phases (or their linear combinations, e.g., Ref. [61]), requiring $p\Delta\mu_A + q\Delta\mu_B + r\Delta\mu_C < \Delta H$ (any competing phases with composition $p:q:r$ of $A:B:C$).

To illustrate how such bulk calculation provides important clues about nonstoichiometry consider the following:

(i) By identifying the structural differences between the target structure (ABC) and its nearest competing phase (e.g., AB_2C), one can determine the type of defect this competing phase will produce. Here, the interstitial B atom is the likely defect that accommodates the off-stoichiometry in cases where the full-Heusler AB_2C is the nearest phase to ABC in the chemical potential diagram (e.g., the first row in Fig. 3).

(ii) Depending on the relative location of the ABC stability region (shaded colored area in Fig. 3) with respect to the full triangle frame, the stability fields for 12 compounds can be categorized into the B -rich (green shading) or C -rich (and A -poor, yellow shading) conditions in Fig. 3.

(iii) The relative size of the allowed zone (colored region in Fig. 3) indicates the ease or difficulty to synthesize the target ABC compound.

(iv) The competing phases neighboring the ABC stability region (Fig. 3) are likely the secondary phases that could appear in the sample during growth. This is especially appropriate when the competing phase has similar structural framework as the ABC half-Heusler compound (e.g., full-Heusler AB_2C materials).

C. Validation via explicit defect calculations

Figure 4 shows our calculated concentration of the main defects (each summed over all of its charge states), as obtained from actual defect calculations in which the defect formation energy is computed for supercells containing one charged defect at the time. Details of the calculation will be further described in Sec. IV A below. We can see from Fig. 4 that, indeed, in the compounds with $B = 3d$ element (ZrNiSn and ZrCoSb), the B interstitials (Ni_i and Co_i) have the highest concentration at B -rich conditions and in the compounds with $B = 5d$ element (ZrIrSb and ZrPtSn), the C -on- A antisites (Sb_{Zr} and Sn_{Zr}) are predominating defects, and the C -on- B and C interstitial defects in ZrIrSb or ZrPtSn all have low concentration. Our defect calculations predict a maximum of 0.6% Ni interstitial surplus at Ni-rich condition in ZrNiSn, a maximum of 1.3% Zr deficiency (V_{Zr}) at Zr-poor and Co-poor conditions in ZrCoSb (Fig. 4). The maximal Sn-on-Zr defect content reaches 3.3×10^{-5} in ZrPtSn at the Sn-rich condition and 6.6×10^{-6} in ZrIrSb at the Sb-rich condition. Note that these off-stoichiometries were predicted using equilibrium

chemical potential conditions within the compound stability field (Fig. 3). This validates the connection between defect-free chemical potential calculation (Fig. 3) and defect calculations (Fig. 4) in terms of identifying the leading defects in these systems due to natural off-stoichiometry.

D. The symmetry of the coordination shells around lattice sites provides additional clues on the leading coordination-preserving point defects

Figure 2(b) shows the coordination shell structure of various sites in the FTS lattice.

1. Antisite defects of A -on- C and C -on- A are energetically likely; the B antisite defects are less likely

The A and C atoms have the same first shell local structure, namely $A[B_4, V_4](C_4)$ and $C[B_4, V_4](A_4)$, respectively, where the square and round brackets denote the first and second nearest neighbors, respectively. These crystallographic factors suggest that A -on- C and C -on- A antisite defects do not change the first shell coordination structure of the lattice. They might be candidates for low formation energy defects provided the atomic sizes are compatible. On the other hand, the B site is eightfold coordinated as in $B[A_4, C_4](V_6)$ so B -on- A , B -on- C , as well as A -on- B , and C -on- B defects would be energetically less likely because such substitutions do not conserve coordination. Our calculated formation energies discussed in Sec. IV confirm such qualitative expectations based on Fig. 2.

2. The B interstitial is likely, whereas A or C interstitials are less likely

Figure 2 shows similarity in coordination shell structures surrounding the B -site and the vacant interstitial site denoted by V . The ideal coordination shell structure around substitutional B is $B[A_4, C_4](V_6)$ and that around V is $V[A_4, C_4](B_6)$. Thus, when the B atom forms an interstitial by occupying the vacant V site, it will create the local structure $B[A_4, C_4](B_6)$, which retains the first neighbor shell as in the ideal substitutional B structure and perturbs only the second shell. In contrast, the shell structure surrounding substitutional A is $A[B_4, V_4](C_4)$, so if A becomes interstitial on the vacant V site, it will create the $A[A_4, C_4](B_6)$ local structure distinct from the ideal local environment of substitutional A . Similarly, the ideal local environment of the substitutional C site is $C[B_4, V_4](A_4)$, so if C becomes interstitial on the V site, it will again create a local environment $C[A_4, C_4](B_6)$ that differs substantially from its ideal neighboring structure. This analysis points to the propensity of B to become interstitial (if size consideration permits), whereas that of A or C interstitials would perturb the local coordination structure too much. Indeed, such qualitative chemical analysis is supported by our calculated formation energy discussed in Sec. IV. The effects of impurity on bond lengths of half-Heusler structures will be quantified in Appendix.

IV. RESULTS: DEFECT CALCULATIONS ON ABC COMPOUNDS

A. Outline of the salient features of the method: Defect formation energy, charge transition energy, equilibrium Fermi energy, and carrier concentrations

The central quantities calculated here are (i) the defect formation energies $\Delta H(D, q, \mu_\alpha, E_F)$ for various charge states q , chemical potentials μ_α , and Fermi energy value E_F and (ii) the defect charge transition levels $\varepsilon(D, q|q')$ between charge states q and q' .

The formation energy $\Delta H(D, q, \mu_\alpha, E_F)$ for defect D in charge states q depend linearly on the atomic chemical potential $\{\mu_\alpha\}$ and the position of the Fermi level E_F (computational details in Appendix). Shown in Fig. 6 are the calculated formation energies for the dominant defects in four half-Heuslers. They can be used to obtain the charge transition levels of a specific defect, which is defined as the Fermi energy E_F^* , at which two charged states q and q' have equal formation energy $\Delta H(D, q, \mu_\alpha, E_F^*) = \Delta H(D, q', \mu_\alpha, E_F^*)$. This gives $\varepsilon(q|q')$, the transition levels, which are shown in Fig. 6 as circles connecting two charge state lines and in Fig. 7 as “levels” in the band gaps. The transition levels do not depend on chemical potential. This calculation incorporates structural relaxations in each charge state. Generally speaking, defect D is ineffective in producing carriers if its donor level is inside the valence band $\varepsilon(+1/0) < 0$ or if the acceptor level is inside the conduction band $\varepsilon(0/-1) > E_g$. More computational details can be found in the Appendix.

The equilibrium Fermi level E_F^{eq} is the key to determine the defect and charge carrier concentrations. This involves a self-regulating feedback effect requiring self-consistency: Take ZrNiSn for an example [Fig. 6(a)]: Electron doping via Ni interstitials raises the Fermi level E_F towards CBM; however, this will decrease ΔH of hole producer (V_{Zr}^{1-}), meaning more holes will form, which compensate electrons, shifting E_F back to lower values. This creates a negative feedback loop. Eventually, the Fermi level will be pinned, and further electron doping becomes impossible. In ZrNiSn, the equilibrium E_F (for details in the Appendix) is drastically enhanced from $E_C - 0.22$ eV to $E_C + 0.01$ eV at the most B-rich (i.e., Ni-rich) chemical condition, indicating a strong n type. For ZrPtSn, the decrease in equilibrium E_F is only minor, creating a weak p type. The same self-regulating mechanism for charge compensation applies also to external impurity doping, such as Sb-doped ZrNiSn (n -type) and Sn-doped ZrCoSb (p -type), where equilibrium Fermi level E_F^{eq} can be determined via the same self-consistent approach (Fig. 8).

Figure 6 shows the formation energy of the leading defects versus parametric E_F for dominant defects and also indicates the equilibrium E_F^{eq} ($T, \{\mu_\alpha\}$) (at growth condition) by a vertical arrow. For ZrNiSn and ZrCoSb, the equilibrium Fermi level is located close to CBM, demonstrating these are n -type materials. In ZrPtSn, the Fermi level is pushed to the midband gap, and the material only display a weak p type. In ZrIrSb, the E_F^{eq} is pinned slightly greater than the $(+1/-1)$ transition level of the Sb-on-Zr defect in the midgap, producing again weak p -type carriers. This is the case in which a single defect (Sb_{Zr}) self-compensates and pins E_F^{eq} .

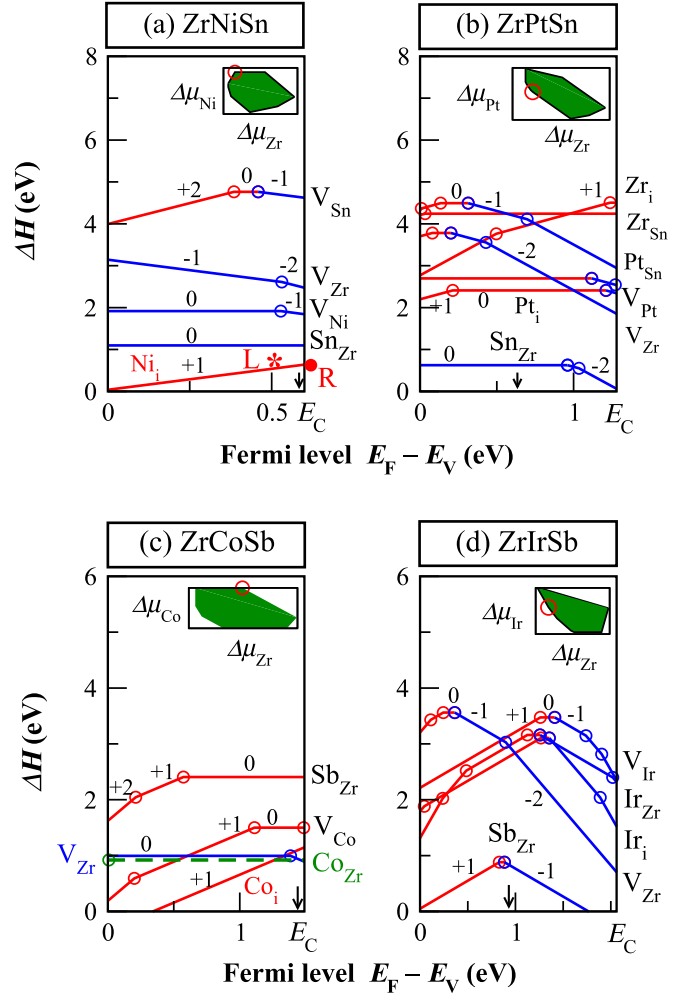


FIG. 6. Formation energy [Eq. (A1) in Appendix] of the dominant defects versus parametric Fermi level in representative IV-X-IV (ZrNiSn and ZrPtSn) and IV-IX-V (ZrCoSb and ZrIrSb) half-Heusler FTS compounds from hybrid functional calculations. The main panel: positively charged electron-donor defects shown in red and negatively charged electron-acceptor defects shown in blue; their charge states denoted in numbers, and their charge transition levels shown in open circles. The Fermi level, VBM, and CBM variables are denoted by E_F , E_V , and E_C , respectively. The inset shows the allowed chemical stability fields (green zones from Fig. 3), whereas the red circle shows the specific chemical condition used for the current ΔH versus E_F calculations. The small vertical arrows indicate the position of the equilibrium Fermi level at growth condition ($T_g = 850^\circ\text{C}$).

1. Defect concentration and carrier density

Figure 4 illustrates the dominant defect concentration, summed over their charge states. Detailed information on dominant defect concentrations in different charge states are shown as a function of chemical condition in the Appendix. Of particular importance is the isosurface plot of majority carrier density versus chemical condition, which reinforces the concept of how chemical conditions influence pertinent defects formation, which, in turn, controls carrier generation.

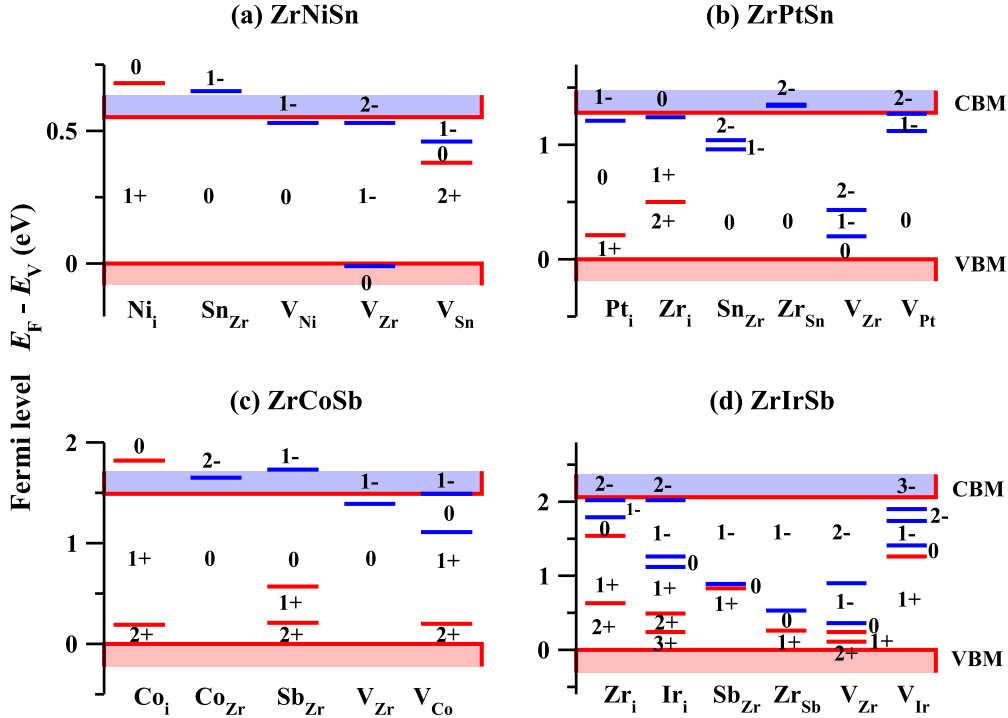


FIG. 7. Charge transition levels [Eq. (A2) in Appendix] of the dominant intrinsic defects in representative IV-X-IV (ZrNiSn and ZrPtSn) and IV-IX-V (ZrCoSb and ZrIrSb) half-Heusler FTS compounds. The donor transition levels are shown in red, and the acceptor levels in blue. The red and blue shadings represent valence and conduction bands, respectively. Shallow donors are those red lines whose (+1/0) transition levels lie above or near E_C (e.g., Ni_i and Co_i), while shallow acceptors are those blue lines with (0/-1) transition level close to E_V (e.g., V_{Zr} in ZrNiSn).

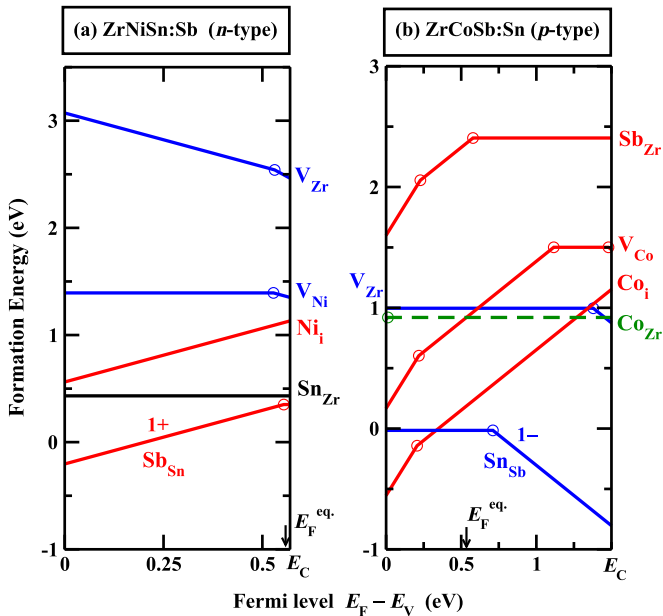


FIG. 8. Formation energy of dominant defects in (a) Sb-doped ZrNiSn at Sb-rich and Ni-poor condition (left panel), and (b) Sn-doped ZrCoSb at Sn-rich and Co-rich condition (right panel) from HSE calculations in a 48-atom supercell. The equilibrium Fermi level at growth condition ($T_g = 850^\circ\text{C}$) is indicated by arrows.

2. The proposed carrier doping rule

The 18 valence-electron ABC compounds with the $B = 3d$ element exhibit n -type carriers because of B excess stoichiometry, which promotes B interstitials that ionize to form donors. The ABC compounds with $B = 5d$ elements are prone to be p -type materials owing to the predominance of C -rich chemical condition, which promotes C -on- A antisite defects that act as acceptors to produce holes. A summary of the doping trend in a few prototype ABC compounds is presented in Appendix.

B. The origin of n -type carriers in ABC compounds with $B = 3d$: ZrNiSn and ZrCoSb

1. Effect of charge neutral Ni concentration on the band gap: Impurity band and the impurity-perturbed conduction band

The contrast in the electronic band structure and the projected Ni 3d density of states between charge neutral $\text{ZrNi}_{1+x}\text{Sn}$ with Ni excess ($x = 6.25\%$) and Ni stoichiometric ($x = 0$) is illustrated in Fig. 5. The presence of Ni_i⁰ reduces the band gap by two effects—forming localized Ni_i⁰ states above the VBM and creating a PHS below CBM. The spin-up and spin-down density of states of Ni_i⁰ state show full spin compensation [Fig. 5(b)]. The major part of the t_2 states are resonant in the valence band, while a majority of e states form in-gap states. The PHS [the green curve in Fig. 5(a)] results from a split down of the Zr- d states at the CBM, because the Ni impurity perturbs the Zr atom coordination shell from $\text{Zr}[\text{Ni}_4, \text{V}_4]\text{Sn}_6$ [Fig. 2(b)] to $\text{Zr}[\text{Ni}_5, \text{V}_3]\text{Sn}_6$, forming a ZrNi_5

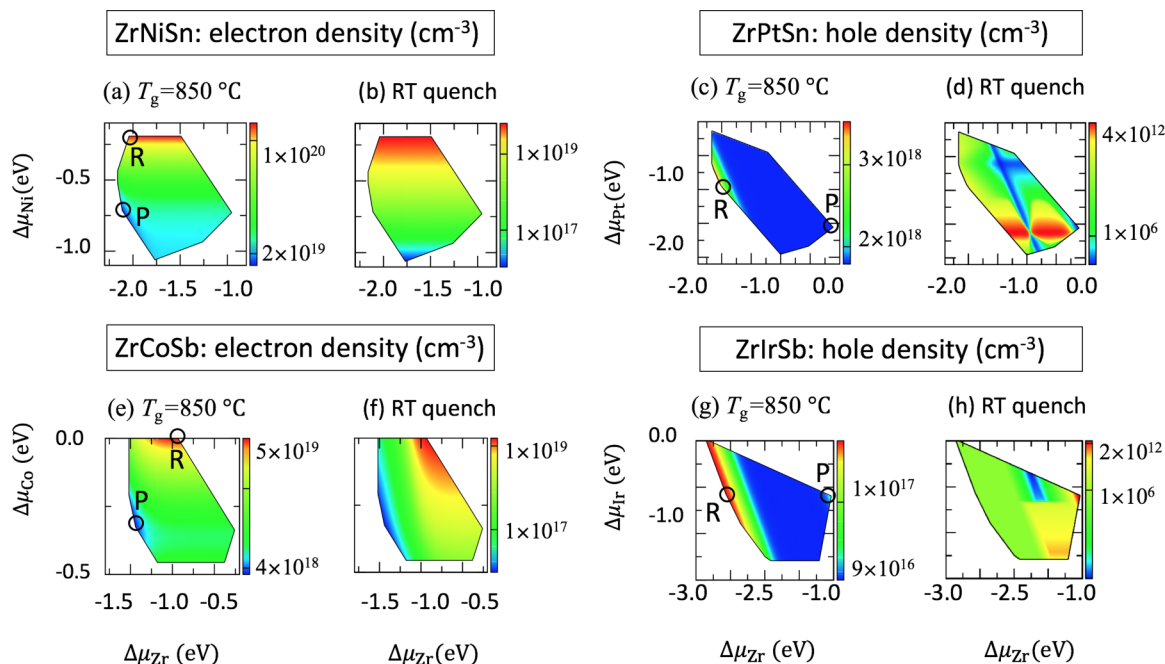


FIG. 9. Isosurface plot of the majority carrier concentrations as a function of excess chemical potentials of A and B elements within the allowed stability triangle region for four half-Hausser compounds: ZrNiSn (a) and (b), ZrPtSn (c) and (d), ZrCoSb (e) and (f), and ZrIrSb (g) and (h). The results are shown at two temperatures: at growth condition ($T_g = 850^\circ\text{C}$) and at room temperature from quench after growth. The letters R and P denote the chemical potential condition, where high and low majority carrier concentration occurs, respectively. R and P represent, respectively, B -rich and B -poor condition for $B = 3d$ compounds—ZrNiSn and ZrCoSb; C -rich and C -poor conditions for $B = 5d$ compounds—ZrPtSn and ZrIrSb.

cluster. Support for band gap closure in $\text{ZrNi}_{1+x}\text{Sn}$ ($x = 25\%$) is presented in Appendix. Besides Ni interstitials, the usual band gap renormalization by temperature (an electron phonon effect) is another factor that reduces band gaps, as in In_2O_3 [62] and ZnO [63].

2. Equilibrium concentration of Ni interstitials

In thermal equilibrium, when all competing intrinsic defects and their charge states were taken into account, we find [e.g., Fig. 4(a)] that the Ni interstitial density reaches a maximum of 0.6% at the most Ni-rich chemical condition and drops down by three order of magnitude at the Ni-poor condition. The experimentally observed 2–6% excess Ni in typical ZrNiSn samples (e.g., Ref. [47]) is most likely due to nonequilibrium growth and the presence of minor phases, such as full-Heusler. The calculated excess Ni concentration (analogous to the calculated Zn concentration out of equilibrium in Perkins *et al.* [64] for Co_2ZnO_4) would increase when adopting out of equilibrium Ni chemical conditions.

3. Ionization of Ni interstitials: In-gap level or resonant in the conduction band and the accuracy limitations of current functionals

Having a full shell $3d^{10}$ configuration, the Ni atom at normal chemical environment may be thought to be inert having high ionization energy, thus, would not act as electron donors. Our spin polarized HSE calculation shown in Fig. 5 indicates that the Ni_i^{1+} exhibits strong exchange splitting between majority and minority spin channels, and the net magnetic

moment is about $0.8 \mu_B$. Electron density analysis reveals 70% of the ionized state in Ni_i^{1+} resulting from the $x^2 - y^2$ orbital, with the rest being delocalized s and p states. Due to exchange interaction, the spin-majority density state [Fig. 5(b)] in Ni_i^{1+} is shifted downwards in energy and hybridize with the valence band, which explains the low formation energy of the approximate d^9 configuration of Ni_i^{1+} .

There are generally two possible types of electron donors:

(i) A *resonant* donor whose $(0/+1)$ charge transition level lies above CBM. Like a metal, this defect system completely ionizes upon formation and shows metallic resistivity behavior with positive $d\rho/dT$. An example is Sb-doped ZrNiSn, as shown in Fig. 8 (a positive $d\rho/dT$ was observed from experiment at doping level 0.5% [65]).

(ii) A *gap level* donor state whose ionization requires activation, so the carrier density increases with T . Such a system can only partially ionize and is characterized by a semiconductor behavior with a negative resistivity versus temperature slope.

Even state of the art defect calculations to date can have an uncertainty of ~ 0.1 eV in the donor transition level in terms of exchange and correlation and thus could spuriously switch between case (i) and case (ii) above. In particular, defect calculations on materials with small band gaps (e.g., ZrNiSn, ~ 0.55 eV gap) are a challenge, due to uncertainties in electronic structures associated with band edges and with defect states. The plain GGA calculations (see Appendix) predict a deep donor level in the gap and thus a significantly low n -type carrier density in ZrNiSn ($< 10^{14} \text{ cm}^{-3}$ at room temperature) due to dominance of charge neutral Ni interstitials. The HSE

functional (mixing 25% of exact exchange) predicts a higher ionization level for Ni interstitial, above the CBM [Fig. 6(a)], due to effect from enhanced Hartree-Fock exchange. However, the 25% of exact exchange is only an approximation used to eliminate self-interaction corrections. We feel that our uncertainty for the Ni (0/+1) charge transition level can be 0.1 eV, considering the effect of exchange on band gap opening and on eigenvalues of in-gap states. We, therefore, consider two computational scenarios allowing for 0.1 eV uncertainties, as shown by point *R* and *L* in Fig. 6(a). The two scenarios lead to completely different physical behavior in temperature dependence of carrier density. In case (i), the Ni interstitial completely ionizes and its (+1/0) transition level is above the CBM [the *R* point in Fig. 6(a)]. Thus, the *n*-type carrier density remains nearly constant with temperature ($\sim 1 \times 10^{20} \text{ cm}^{-3}$, the dashed red line in Fig. 10). While in case (ii), the Ni interstitial (+1/0) transition level lies slightly below the CBM [e.g., $E_{\text{CBM}} - 0.07 \text{ eV}$, the *L* point in Fig. 6(a)], the Ni interstitial only partially ionizes due to thermal excitations ($\sim 10\%$ of Ni interstitials ionize at room temperature from simulation); therefore, the carrier density increases almost linearly with temperature (the solid red line in Fig. 10). When the donor is resonant, we predict a high carrier density in ZrNiSn (10^{19} cm^{-3} at room temperature). This result from case (ii) is consistent with the observed linear *T* dependence of the electrical conductivity in undoped ZrNiSn samples [43,66], so it is the preferred scenario.

4. Magnetism of ionized interstitial Ni

Ni interstitials have the potential to create magnetic moments in both fully ionized and partially ionized cases. As a magnetic impurity, the Ni interstitial possesses a localized moment of $\sim 0.8 \mu_B$ from the $x^2 - y^2$ $3d$ orbital. For magnetism in the dilute doping limit, it was known that doping concentration has to exceed the three-dimensional (3D) percolation threshold for the specific lattice before the itinerant ferromagnetic properties can set in [67]. Below the percolation threshold, the magnetic impurities form small clusters, and they behave like superparamagnetic states. It could be possible to observe such phenomena in delicately controlled off-stoichiometric samples.

5. The *n*-type doping in ZrCoSb

Like Ni_i , the Co_i in ZrCoSb is a shallow donor, but the ionized donor electrons originate from a delocalized wave function in the charge neutral state (mainly, *s* and *p* characters), with the eigenvalue lying above the CBM. In contrast, the Pt interstitial in ZrPtSn ($B = 5d$) has a deep donor transition level (+1/0) close to VBM (Fig. 7b), while Ir interstitial in ZrIrSb ($B = 5d$) shows bipolar behavior with donor (+1/0) and acceptor (0/1-) levels both lying close to the middle of the band gap [Fig. 7(d)].

The *Co* vacancy in ZrCoSb possesses a shallow donor transition (+1/0) at $E_V + 1.1 \text{ eV}$ [or $E_C - 0.4 \text{ eV}$, Figs. 6(c) and 7(c)]. With an odd number of electrons, V_{Co}^0 state shows a magnetic moment of $1.3 \mu_B$ (HSE results), which is delocalized and uniformly distributed on the four tetrahedral Zr atoms that contract towards the vacancy center. When it ionizes, the V_{Co}^{1+} state, having an even number of electrons, shows

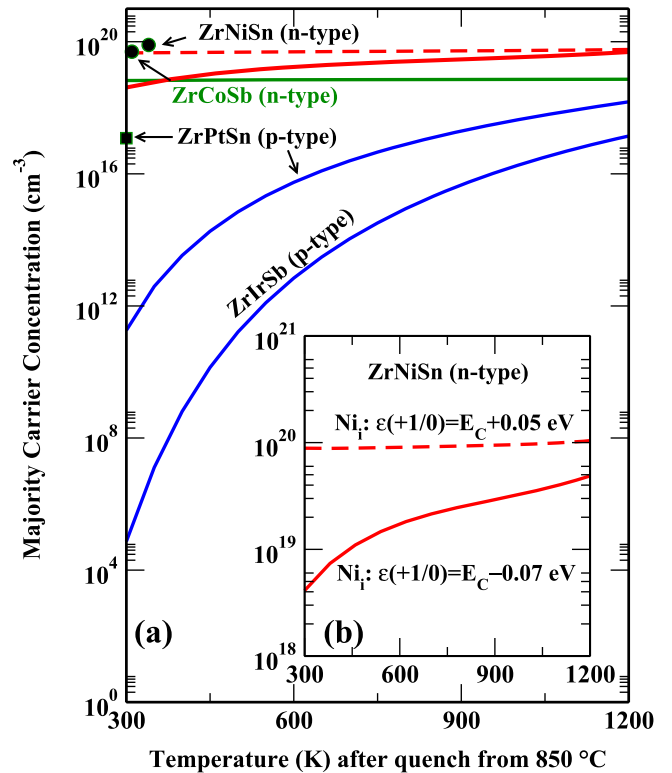


FIG. 10. (a) Majority carrier density versus quench temperature after growth from 850 °C for the *n*-type and *p*-type $A^{\text{IV}}BC$ compounds at *B*-rich and *C*-rich chemical conditions, respectively. The black dots denote experimental measured values for ZrNiSn [43], ZrCoSb [68], and ZrPtSn [69]. For ZrNiSn, the solid red and dashed red curves represent calculations based on two scenarios exemplified in the inset figure. (b) The *n*-type carrier density in ZrNiSn calculated from two scenarios: (i) Ni interstitial being fully ionized, the ionized state being a resonant state in the conduction band, as shown from point *R* in Fig. 6(a). This leads to a nearly constant carrier density versus *T* as shown in the dashed red line. (ii) Ni interstitial being partially ionized, with the ionized state staying within the band gap as shown from point *L* in Fig. 6(a). This leads to a sublinear relation between carrier density versus *T*, as shown in the solid red curve, which is consistent with the negative dp/dT observed from experiments (e.g., [43,66]). In general, the quench temperature has little effect on *n*-type carriers but strong effect on *p*-type carriers. This is because in *n*-type $A^{\text{IV}}BC$, carrier-producing charged defects (*B* interstitial 1+) dominate all other charged defects, while in the *p*-type $A^{\text{IV}}BC$, there is strong competition between the carrier producing charge states (*C*-on-*A* antisite $q = 1-$) and others, e.g., *C*-on-*A* antisite ($q = 0$ and 1+) charge states in ZrIrSb and *B* interstitial ($q = 1+$) in ZrPtSn.

no net spin moment on any atom; hence, it is energetically more favorable. The same concept concerning the magnetic moment versus odd number of electrons applies to Ni vacancy, explaining why V_{Ni}^0 wins over V_{Ni}^{1+} or V_{Ni}^{1-} , the opposite of the V_{Co}^0 case.

6. Summary of the origin of *n*-type carriers in ABC compounds with $B = 3d$

The *big picture* that emerges is that for the compounds containing $3d$ elements in the *B* position (ZrNiSn and

ZrCoSb), the bulk solids are naturally $3d$ rich and the leading electron-producing donors are consistently the $B = 3d$ interstitials, which have low formation energy and a shallow donor transition level ($0/1+$). The potential electron killers (V_{Zr} , Sn-on-Zr or Sn-on-Sb) are ineffective, having either a high formation enthalpy (A vacancy) or deep level (C -on- A antisite). The absence of effective electron killers opens the door in these systems not only for off-stoichiometry doping but also for effective *impurity donor doping*. For example, we find that Sb doping in ZrNiSn readily produces a high electron carrier density (10^{20} cm^{-3} at room temperature from quench) due to the $(\text{Sb-on-Sn})^{1+}$ defect, reflecting the absence of any strong compensating acceptor.

C. The origin of p -type carriers in ABC compounds with $B = 5d$: The cases of ZrPtSn and ZrIrSb

1. Interpretation of p -type ZrPtSn, HfPtSn, ZrIrSb, TaIrGe, LnPdSb ($Ln = Y, Ho, Er, La, Gd$) and LnPdBi ($Ln = Nd, Y, Dy, Ho, Er, La, Gd$)

There exists sporadic experimental evidence for p -type half-Heuslers (mostly thermoelectric materials), such as ZrPtSn, HfPtSn, ZrIrSb, TaIrGe, YPtSb [57], LnPdSb ($Ln = Y, Ho, Er, La, Gd$) [58], and LnPdBi ($Ln = Nd, Y, Dy, Ho, Er, La, Gd$) [59], yet the origin of p -type carriers was unknown.

The exchange or atomic disorder between A and C sublattice sites does not introduce carriers, thus, cannot be the cause. Our results points to a different explanation: *the negatively charged C-on-A antisite defects form spontaneously and create holes in the ABC compounds with $B = 5d$ elements at favorable chemical conditions*. This conclusion is reached from the following physical analysis and verified from thorough defect calculations.

a. Hole producing defects consistent with C-rich conditions. In the ABC compounds containing $5d$ elements in the B position (ZrPtSn and ZrIrSb, for instance), the bulk solids contain stability fields that are naturally C rich and A poor (Fig. 3), favoring C -on- A antisite defects rather than B interstitials. The other potential defects that could be accommodated by the C -rich condition, such as C -interstitial and C -on- B defects, are excluded due to violation of local CN, thus having high formation energy. The negative charge state in C -on- A defects is critical to produce holes. The hole producers can have low formation energy: In the case of ZrPtSn, the Sn-on-Zr antisite ($2-$), and in the case of ZrIrSb the Sb-on Zr antisite defect ($1-$), and in the cases of TaIrGe the Ge-on-Ta antisite ($1-$; all C -on- A defect) are the primary hole producer, *all with low formation energies*.

b. Potential hole killer defects. At the same time, at Sn-rich condition, all hole killer defects in ZrPtSn have high formation energy, thus, ineffective, including Pt_i , which is a deep donor and Zr_i , which is a shallow donor [Fig. 6(b)]. In ZrPtSn and ZrIrSb, however, *the relevant acceptors are deep* [Figs. 6(b), 6(d), 7(b), and 7(d)]. This indicates that the p -type character in these two compounds is *latent*, being manifest only at high temperature but insignificant at room temperature (Fig. 9). The metal vacancy (V_{Zr}) having high formation energy serves only as the secondary hole producer, even though it is a shallow acceptor. In contrast, while TaIrGe [14] also has low formation energy for the hole producer Ge-on-Ta antisite, the

acceptor level is shallow (see Appendix), so this system is a p type not a latent p type. As a result, TaIrGe shows relatively high p -type carrier concentration at room temperature after quench from growth [experimental value: $0.8 \times 10^{15} \text{ cm}^{-3}$; see Fig. 4(b) in Ref. [14]].

In addition, there are no effective donors to kill holes, since (a) the B -rich chemical condition is not available to support B interstitial and (b) the B atom is rather large so the B interstitial (Pt_i and Ir_i) becomes energetically unfavorable. As expected from the symmetry discussion in Sec. III B, Zr_i has also high ΔH , thus will not introduce carriers even though its transition level can be shallow. Thus, there is no effective electron producers/hole killers.

2. A single bipolar Sb-on-Zr antisite defect

A very special case is ZrIrSb, an ABC compound with $B = 5d$ Ir element, where the charged carrier compensation occurs mainly due to a single bipolar Sb-on-Zr antisite defect (Figs. 6 and 7), which is capable of acting as both acceptor (-1) and donor ($+1$). The charge transition level ($+1/-1$) lies in the middle of the band gap but closer to VBM. Since all hole-killer defects (electron donors) have high formation energy, e.g., Ir_i and Zr_i , it is the Sb-on-Zr defect itself that determines the net hole concentration. The equilibrium Fermi level is pinned slightly above the ($+1/-1$) transition level, which is in the midband gap. Hence, ZrIrSb can be regarded as a latent p -type compound, in which the hole carrier concentration is high at growth condition (e.g., 850°C), but low at room temperature (Fig. 9).

3. Summary of origin for p -type carriers in $B = 5d$ elements in ABC compounds

The *big picture* that emerges is that for the ABC compounds containing $5d$ elements in the B position (e.g., ZrPtSn and ZrIrSb), the bulk solids contain stability fields that are naturally C rich and A poor, favoring C -on- A antisite defects rather than B interstitials. The C -on- A antisite defects are prone to form acceptors (producing holes), which can be rationalized by the strong electron negativity of IVA and VA elements (e.g., Sn and Sb) versus the weak electron negativity group of IIIB, IVB, and VB group (e.g., Y, Zr, Ta). Furthermore, shallow donors, such as B interstitials and A interstitials, become energetically unfavorable at the preferred chemical conditions (C rich). Hence, no prevalent electron producers exist to kill holes.

D. Impurity chemical doping in $B = 3d$ ABC compounds

1. The Sb-doped ZrNiSn (n type)

Note that when we study impurity doping by Sb-doped ZrNiSn, we find shallow donor states with the ($0/1+$) ionization level lying above the CBM, as shown from the HSE calculation (Fig. 8). This is a resonant donor case with predominantly low formation energy. The absence of any effective electron killer in ZrNiSn also benefits the n -type behavior. Experiments illustrate metallic behavior in the Sb-doped ZrNiSn samples (Sb: at 0.5%) with the usual positive $d\rho/dT$ relationship [43], which is consistent with this calculation.

2. The Sn-doped ZrCoSb (*p* type)

HSE results show that Sn-on-Sb is the dominant defect, having the lowest formation energy, but its acceptor transition level (0/1-) is rather deep (Fig. 8). Hence, the resulting hole concentration is low at room temperature and relatively high only at growth condition, 850 °C. This case illustrates a *latent p-type compound*, dominated by an uncompensated, deep, hole producer with low formation energy (Sn-on-Sb antisite defect), which can only generate small amount of hole carriers at room temperature (see Appendix for details).

E. Effect of A atom selection in ABC compounds with either $B = 3d$ or $B = 5d$ elements (the IV-X-IV and IV-IX-V groups)

Although we expect an approximately similar carrier doping behavior in the group of A^{IV} NiSn, A^{IV} PtSn, A^{IV} CoSb, and A^{IV} IrSb compounds with $A^{IV} = \text{Ti}$ and with $A^{IV} = \text{Zr}$ group, we are aware of the difference among the two groups. The chemical stability field of the $A^{IV} = \text{Ti}$ group, as shown in the first column of Fig. 3, appears to be larger in area and more extended to the A-rich condition than its $A^{IV} = \text{Zr}$ and Hf counter parts. Recently, Wambach *et al.* [36] measured the thermopower factor in the Ti-Ni-Sn compositional space using thin film growth technique with combinatorial approach. Three major off-stoichiometry were observed in the thin film system, which might have shown metastable characters: Ni surplus in TiNiSn + TiNi₂Sn assemblage, Ti surplus and Ni surplus in TiNiSn + Ti₂Ni₂Sn aggregate, and Sn surplus in the TiNiSn + Sn two phase region. This is consistent with our chemical potential diagram (Fig. 2), where the stability field of TiNiSn is constrained by the Heusler phase TiNi₂Sn in the Ni-rich condition and Ti₂Ni at the Ti-rich condition. The stability field of Ti₂Ni₂Sn phase is nearly touching the boundary of TiNiSn at the Ti-rich and Ni-rich condition. Note the errors in the defect calculations of Wambach *et al.* [36]. The full-Heusler phase (TiNi₂Sn) is missing in the chemical stability field, which contradicts experiment, and defects with the charge neutral and acceptor states (negative charge) were not included in their calculation, which would lead to inaccurate results on carrier density and defect concentrations.

F. Defect and carrier density study: The effects of chemical condition, growth, and quench temperatures

To simulate carrier concentrations in samples at quenched temperature after growth or prolonged annealing (e.g., at 850 °C), we assume that the atomic local structures associated with defects are frozen in at high T growth condition, while ionization states of defects and free carriers re-equilibrate at low temperature to preserve the charge neutrality condition. When applying this method to study variation of carrier density with chemical condition (Fig. 9) and temperature (T at quench from growth, as in Fig. 10), we find that for ZrNiSn and ZrCoSb:

(i) The n -type carrier concentration exhibits maximum at B -rich chemical conditions (Ni rich and Co rich, respectively, Fig. 9), consistent with the observed coexisting Ni and Co metal phase in experiment.

(ii) The carrier concentration we obtained ($\sim 10^{19} \text{ cm}^{-3}$) at room temperature (quench) agrees with experiments ($\sim 8 \times$

10^{19} cm^{-3} for ZrNiSn [43] and $5 \times 10^{19} \text{ cm}^{-3}$ in ZrCoSb [68], shown in Fig. 10). In ZrNiSn [Figs. 9(a) and 9(b)], the *electron* concentration varies strongly with Ni chemical potential (y axis) but is insensitive to Zr chemical condition (x axis). This creates the horizontal stripe feature in the two-dimensional isosurface, which is due to the negligible contribution to carriers from Zr-related defects, such as V_{Zr} , Zr_i , Sn_{Zr} in ZrNiSn. A similar situation occurs in ZrCoSb [Figs. 9(e) and 9(f)], except having a weaker correlation between the B -rich chemical condition and the stripe feature, which apparently is due to competition from other energetic defects, such as V_{Zr} , V_{Co} , and Co_{Zr} .

(iii) Once quenched from the growth condition (850 °C), the electron carrier concentration remains high and has only mild dependence on temperature in ZrNiSn and ZrCoSb, as shown in Fig. 10. This persistent concentration versus temperature effect is the outcome of one single charged defect (B interstitial 1+) dominating the carrier generation. Examples are Ni_i^{1+} in ZrNiSn, Co_i^{1+} in ZrCoSb (Fig. 5), and $\text{Ge}_{\text{Ta}}^{1-}$ in TaIrGe.

In ZrPtSn and ZrIrSb, due to latent p -type defects (Sn-on-Zr in ZrPtSn and Sb-on-Zr in ZrIrSb), the maximal hole concentration reaches 10^{17} – 10^{18} cm^{-3} at growth condition [Figs. 9(e) and 9(g)]. Upon quench to room temperature, the isosurface map as a function of chemical condition shows nonlinear features, indicating existence of competing p -type defects, while the maximum carrier density plunges to 10^{12} cm^{-3} in both compounds [Figs. 9(d) and 9(h)]. The carrier density at the C -rich condition shows exponential decay with quench temperature, as shown in Fig. 10. In experiment, a medium hole concentration ($1.2 \times 10^{17} \text{ cm}^{-3}$) is found in ZrPtSn samples, where the source of defect is unknown and the Zr:Pt:Sn ratio drifts away from 1:1:1 [69]. ZrIrSb, which was recently synthesized from experiment [13], has a Seebeck coefficient ($44.3 \mu\text{V/K}$) much lower than the TaIrGe sample [14] ($82 \mu\text{V/K}$), with low hole concentration of $0.8 \times 10^{15} \text{ cm}^{-3}$, and a conductivity (6.5 S/cm) much higher than TaIrGe (0.35 S/cm) [14]. Thus, ZrIrSb may also have low hole concentration and high hole mobility, which, however, is not given in experiment [13].

Further defect concentration analysis (Fig. 11) reveals that in ZrPtSn when the chemical potential condition varies from Sn-rich to Sn-poor conditions at growth condition (along the line R-P [rich-poor] in Fig. 9), the amount of Sn-on-Zr acceptor defect falls off exponentially, while the amount of V_{Pt}^{-1} grows up and leads to low hole concentration at Sn-poor condition. Similarly in ZrIrSb, when the chemical condition varies from the Sb-rich to Sb-poor condition, the leading charged defect changes from $\text{Sb}_{\text{Zr}}^{1-}$ to $\text{Zr}_{\text{Sb}}^{1-}$ [Fig. 11(d)]. Once again, this emphasizes the role of chemical potential condition (or off-stoichiometry) on formation of intrinsic (charged) defects in half-Heusler compounds, as discussed in Sec. III.

Comparing the majority carrier concentrations at growth condition [850 °C, Figs. 9(a), 9(c), 9(e), and 9(g)] with those from quench [Figs. 9(b), 9(d), 9(f), and 9(h)] for the four ABC compounds, we find that when a single ionized defect dominates carrier production (Ni_i^{1+} in ZrNiSn and Co_i^{1+} in ZrCoSb), quench to low temperature has only minor effects: reducing maximal carrier concentration by about tenfold and broadening the high carrier concentration regime (n versus $\{\Delta\mu_\alpha\}$ plot) under chemical potential domains that favor

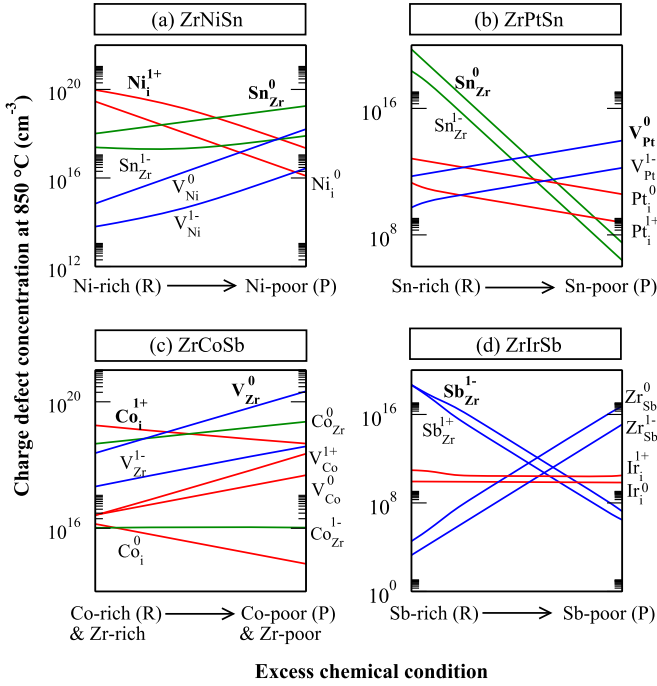


FIG. 11. Variation of dominant charged impurity concentrations in representative half-Heusler compounds at growth condition ($T_g = 850^\circ\text{C}$) along a line of chemical potential conditions (R-P), connecting the rich and poor chemical potential conditions, as shown in Fig. 9. The red, blue, and green colors denote interstitial, vacancy, and antisite defects, respectively.

donor formation. In contrast, the low concentration and the complex topographic feature (Fig. 9) of the quenched carriers in ZrIrSb and ZrPtSn are due to multiple competing defects, such as Sb-on-Zr (1+) versus (1-) in ZrIrSb; Sn-on-Zr (2-, 0), and $\text{V}_{\text{Pt}}(1-)$ in ZrPtSn (Fig. 6).

V. SUMMARY OF THE CONCEPTUAL FRAMEWORK AND ITS BROAD APPLICABILITY

We uncover fundamental trends in the science of carrier doping in half-Heusler FTS compounds $A^{\text{IV}}B^{\text{X}}C^{\text{IV}}$ and $A^{\text{IV}}B^{\text{IX}}C^{\text{V}}$:

(i) Chemical potential diagram can infer the propensity for natural off-stoichiometry in the bulk compound; the latter, in conjunction with crystal symmetry characteristics, can promote preferential defects and suppress unfavorable ones.

(ii) There are four prototype intrinsic doping cases for the $A^{\text{IV}}B^{\text{X}}C^{\text{IV}}$ and $A^{\text{IV}}B^{\text{IX}}C^{\text{V}}$ groups: (a) high n -type due to shallow donors, while killer acceptors are of high energy, e.g., intrinsic ZrNiSn and ZrCoSb and Sb-doped ZrNiSn; (b) latent p -type due to deep acceptor with low formation energy, while killer donors are of high energy, e.g., ZrPtSn and ZrCoSb:Sn; (c) latent p -type due to a single bipolar defect, while killer donors are at high energy, e.g., ZrIrSb; (d) good p -type due to relative shallow acceptor, while killer donors at high energy, e.g., TaIrGe.

(iii) The critical importance of understanding-based design principles for doping compounds is clearly revealed. The conceptual design scheme presented here includes the following steps: (i) identify characteristics in chemical stability fields and

natural off-stoichiometry; (ii) use crystal symmetry analysis and off-stoichiometry to infer dominant charge neutral defects and verify by defect study; (iii) deduce defect compensation scenarios by inspecting ionization levels of all existing defects and their formation energy at all possible chemical potential conditions; (iv) compute carrier density at growth and quench condition throughout the allowed chemical stability field to compare with experiments; and (v) compute the charged defect density in the system to verify the defect compensation scenarios. We feel that these conceptual steps have a broad validity for future defect and carrier-doping studies in various functional materials and for comparison with experiments. Following this design approach will bring the theoretical study on a more comparable level with the experimental results.

ACKNOWLEDGMENTS

At the University of Colorado, Boulder, Y.G.Y., X.Z., and A.Z. were funded by U.S. Department of Energy, Theoretical Condensed Matter Physics, Materials Sciences and Engineering Division, Office of Basic Energy Sciences under Contract No. DE-FG02-13ER46959. This paper used resources of the National Energy Research Scientific Computing Center, which is supported by the Office of Science of the U.S. Department of Energy under Contract No. DE-AC02-05CH11231. We thank J. Snyder for important discussions on experiments, Y. Kimura for discussions on experiments of ZrPtSn, G. Trimarchi for helpful assistance in supercomputer work, and L. Yu for discussions on defect calculations.

APPENDIX: TECHNICAL DETAILS AND SUPPORTING INFORMATION ON THIS CARRIER DOPING STUDY

1. Bulk compounds and their properties

The hybrid functional calculations (HSE) have been performed on 50 cubic 18-valence-electron ABC compounds to reveal a systematic trend in electronic band structure and band gaps (green shaded area in Fig. 12). Note that the noncubic phases are metal. Among the four prototype chemical groups ($A^{\text{IV}}B^{\text{X}}C^{\text{IV}}$, $A^{\text{IV}}B^{\text{IX}}C^{\text{V}}$, $A^{\text{III}}B^{\text{X}}C^{\text{V}}$, and $A^{\text{V}}B^{\text{IX}}C^{\text{IV}}$), we find that (i) the band gap is insensitive to the choice of the A element, i.e., varying the A element across the Ti-Zr-Hf series barely changes band gaps of the compounds (Fig. 12), which is also observed from the similarity of band structures in each row of Fig. 13. (ii) Except for the $C^{\text{V}} = \text{Bi}$ compounds including $A^{\text{III}}B^{\text{X}}C^{\text{V}}$ and $A^{\text{IV}}B^{\text{IX}}C^{\text{V}}$, the band gap of ABC compounds generally widens with an increase of atomic number in B element, such as in the group 10 (Ni-Pd-Pt) and group 9 (Co-Rh-Ir) series (Fig. 12). This is very likely due to the increased band repulsion between the conduction band (the E state from the d electrons in the A element) and the valence band [the T_2 states dominated by the d^9 (Co) or d^{10} (Pt) state in the B atom].

We define three structures for the half-Heusler compounds with the cubic FTS (Fig. 2): the ground state (the α structure) where the group VIII elements occupy the eightfold coordinated site (Ni, Pd, Pt, Co, Rh, Ir), and the β and γ structure, where the other two elements occupy the eightfold site. Calculating the energetics of the three structures for

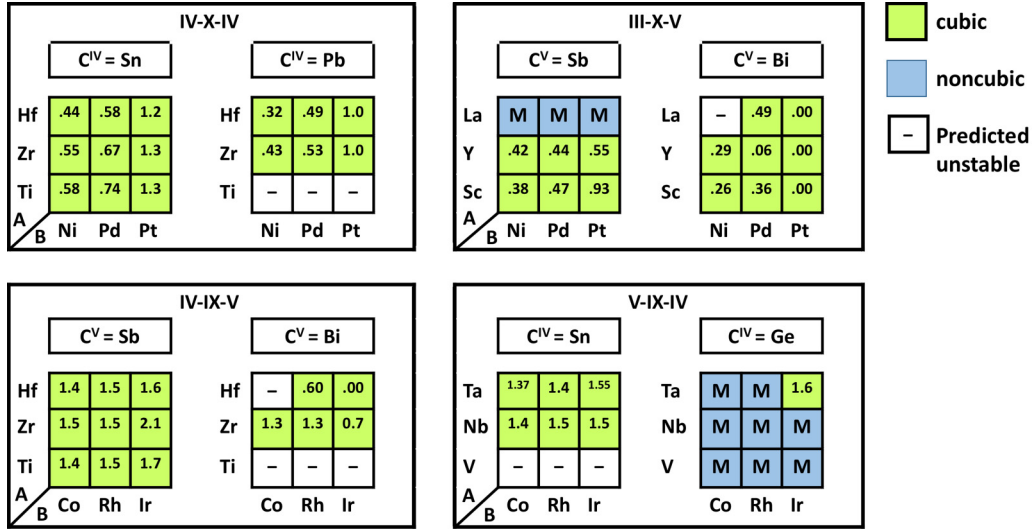


FIG. 12. Fundamental band gaps (in electron volt from HSE calculation) of a group of 18 valence-electron half-Heusler compounds in four prototype chemical groups $A^{\text{IV}}B^{\text{X}}C^{\text{IV}}$, $A^{\text{IV}}B^{\text{IX}}C^{\text{V}}$, $A^{\text{III}}B^{\text{X}}C^{\text{V}}$, and $A^{\text{V}}B^{\text{IX}}C^{\text{IV}}$. The ternary compounds with cubic structure ($F\bar{4}3m$) are nonmetal (shaded in green), whereas those in noncubic structures are metal (shaded in blue). Those that are predicted unstable are denoted by minus sign (-).

50 cubic half-Heusler compounds reveals that the β and γ structures are energetically unfavorable, about 0.7 eV per atom higher than the ground state (Fig. 14), indicating their non-existence.

2. Compound formation enthalpies and competing phases

The fitted elementary reference energy method (FERE [73]) in conjunction with DFT has been successfully applied to compute compound formation enthalpies in cubic half-Heusler compounds and in their computing phases (Tables II and III). The results show significant improvement over the plain GGA calculations, and are subsequently used in carrier doping studies to constrain the chemical potential stability field of the host compound.

3. Concept and computational formula for defects and doping

Defect formation energy is defined as the energy cost to create a point charged defect in an infinite lattice space (i.e., at dilute limit) through exchanging an atom and electron with the chemical reservoir and Fermi sea, respectively. To extract the defect formation energy from a finite supercell calculation, one uses the following formula

$$\Delta H(D, q, \mu_\alpha, E_F) = \{E(D, q) - E_H\} \pm \sum_\alpha (\mu_\alpha^0 + \Delta\mu_\alpha) + q(E_V + E_F) + \delta H_{\text{corr}} \quad (\text{A1})$$

where $\Delta H(D, q, \mu_\alpha, E_F)$ is the formation energy of defect D in charge state q under the condition of elemental chemical potential μ_α and the parametric electronic Fermi energy E_F (relative to the VBM E_V). In addition, $E(D, q)$ is the energy of the supercell containing defect D in charge state q , and E_H is the energy of the host; μ_α is the chemical potential of atoms in the reservoir, which can be decomposed into values for pure elements (μ_α^0) and the excess chemical potential ($\Delta\mu_\alpha$). We will provide in the following section specific details on

the method of calculation, the way finite cell size and DFT errors are rectified to obtain δH_{corr} , the correction to the defect formation energy, and explain how relaxation is taken into account (see Refs. [52,77,78]).

Charge transition level of a specific defect is defined as the Fermi energy E_F^* , at which two charged states q and q' have equal formation energy $\Delta H(D, q, \mu_\alpha, E_F^*) = \Delta H(D, q', \mu_\alpha, E_F^*)$, which has been calculated from Eq. (A1). This gives

$$\begin{aligned} E_F^* &= \varepsilon(D, q|q') \\ &= \frac{\{E(D, q) + \delta H_{\text{corr}}(D, q)\} - \{E(D, q') + \delta H_{\text{corr}}(D, q')\}}{q' - q} \\ &\quad - E_V. \end{aligned} \quad (\text{A2})$$

The transition levels are an intrinsic property for the defect and do not depend on chemical potential.

Equilibrium Fermi level can explicitly determine how much carriers can be doped into the compounds. Enforcing the charge neutrality condition, we have

$$\begin{aligned} \sum_{s=1}^{n \text{ site}} n_s \sum_{D, q} q_{s, (D, q)} \frac{1}{Z_s} \exp(-\beta \Delta H_{\text{form}}(D, q, \{\mu_\alpha\}, E_F)) \\ = \int_{E_C}^{\infty} g(E) f_{\text{FD}}(E) dE - \int_{-\infty}^{E_V} g(E) (1 - f_{\text{FD}}(E)) dE \end{aligned} \quad (\text{A3})$$

Here, E_F is an input continuous formal parameter used to scan $\Delta H(D, q, \mu_\alpha, E_F)$ when $\text{VBM} < E_F < \text{CBM}$, whereas E_F^{eq} is the thermodynamic equilibrium Fermi energy obtained as the output solution. In specific, Z_s is the partition function on site s due to all charge defects competing with the ordered host, i.e., $\text{Tr}(-\beta \Delta H_{\text{form}})$ with $\beta = 1/k_B T$; $g(E)$ is the electronic

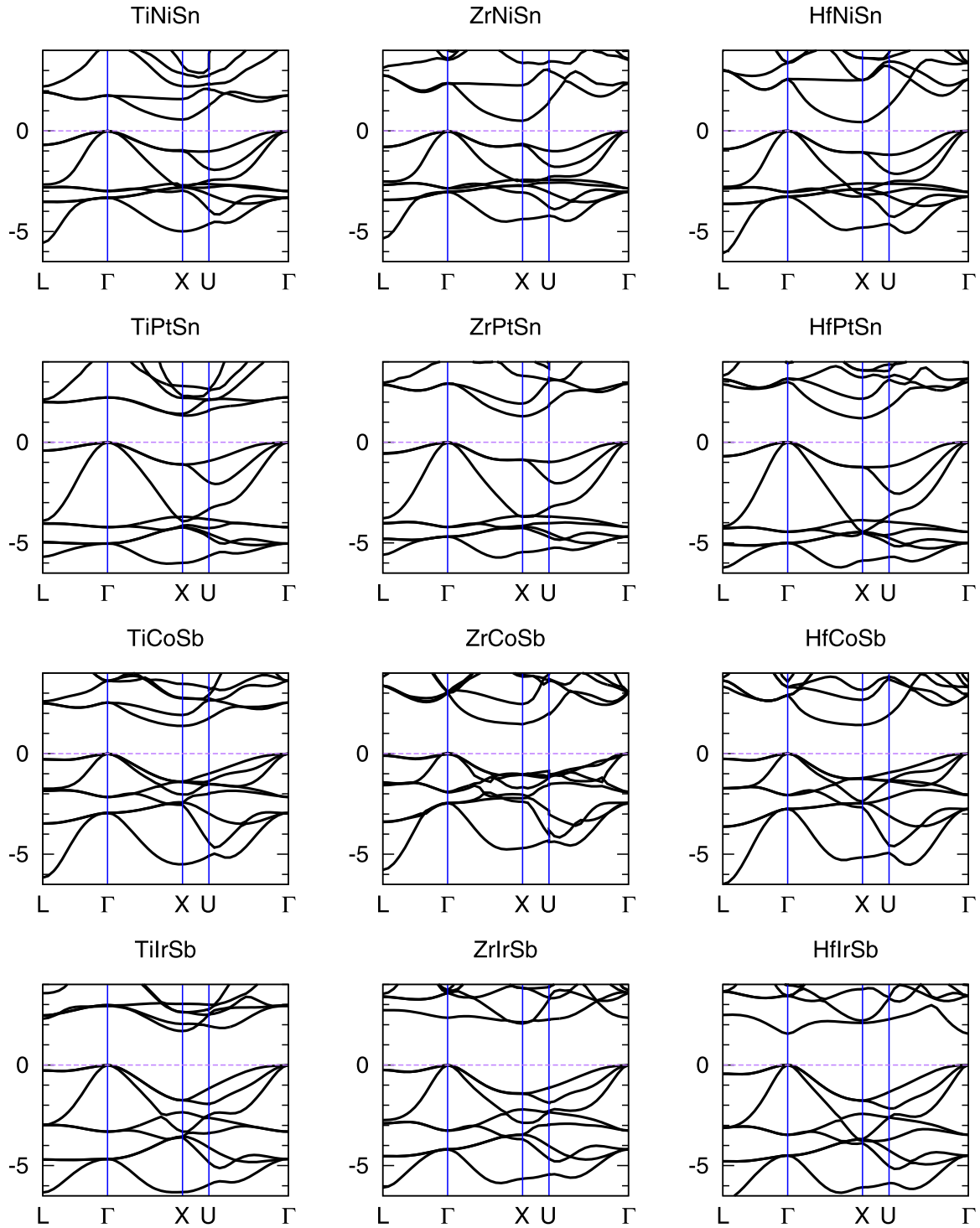


FIG. 13. Electronic band structure of the 12 half-Heusler compounds from hybrid functional calculations (HSE). The energy (eigenvalue) reference is set to E_V , the VBM.

density of state and f_{FD} is the Fermi-Dirac distribution; $\{\mu_\alpha\}$ is the set of chemical potential under which ΔH_{form} is defined; n_s is degeneracy of site s per unit cell. Also, $g(E)$ is the density of states obtained from DFT calculation of the host compound and fitted by cubic spline for an interpolation at the logarithmic energy grid. Clearly, equilibrium E_F depends on chemical potentials and temperature. Figure 21 gives an example of the

calculated equilibrium Fermi energy, as a function of chemical potential and growth temperature.

Defect concentration and carrier density: Once $E_F^{\text{eq}}(T, \{\mu_\alpha\})$ is obtained self-consistently in Eq. (A3), the concentration of each charged defect (D, q) is obtained, as they are the weighted Boltzmann value on the left-hand side of Eq. (A3).

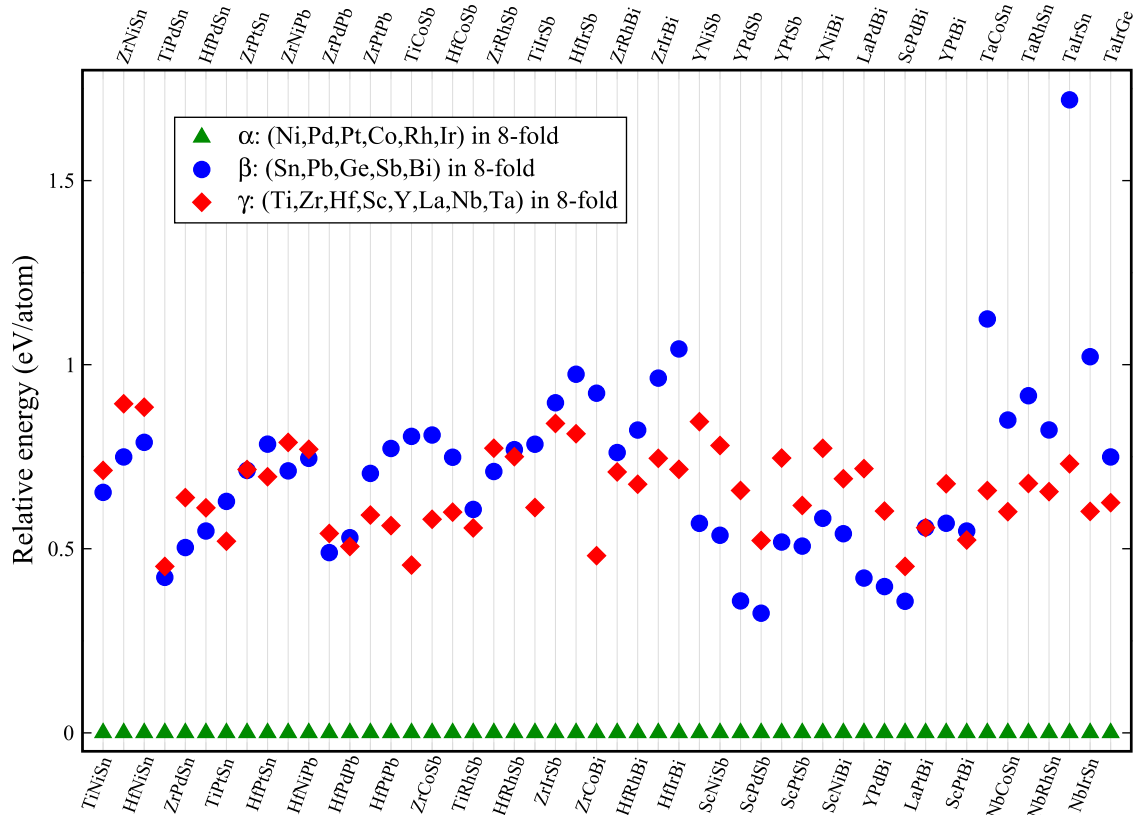


FIG. 14. Relative total energies (electron volt per atom) of the β and γ structures of the ABC compounds with respect to the ground state α phase for the 50 cubic ABC half-Heusler compounds from Fig. 1. In the α structure, the group VIII elements (Ni, Pd, Pt, Co, Rh, Ir) occupy eightfold site and the other two elements occupy the two fourfold sites [see Fig. 2(a)]; in the β structure, the group IVA and VA elements (Sn, Pb, Ge, Sb, Bi) occupy eightfold site; in the γ structure, the group IIIB, IVB, VB elements (Ti, Zr, Hf, Sc, Y, La, Nb, Ta) occupy eightfold site. In all cases, the ground state is the α phase.

4. Computational detail for defects and doping

a. Calculating the $E(D, q) - E_H$ term

The calculation of the $E(D, q) - E_H$ terms needs to benefit as much as possible from cancelation of errors. Therefore, both quantities need to be calculated at the equivalent K point set, basis set size, and other integration grids. We use a bcc-type rhombohedral supercell containing 48 atoms; increasing the supercell dimension to a $2 \times 2 \times 2$ cubic cell containing 96 atoms has small effects, as illustrated in Fig. 15. For the cutoff energy for the plane wave basis set, we use 1.3 times the maximum default cutoff from each pseudopotential in an ABC compound (360 eV maximum). To compute $E(D, q)$ and E_H , we use the pseudopotential total energy and force formalism, the Perdew-Burke-Ernzerhof (PBE) GGA functional and the projector-augmented wave (PAW)-PBE pseudopotential approach, as implemented in the Vienna *Ab initio* Simulation Package (VASP) code [79–81].

b. Postprocessor corrections

The δH_{corr} term expresses the postprocessor corrections, which is necessary to deal with two classes of errors (a) the finite supercell effects and (b) DFT errors. (We emphasize that calculations that omit some of these corrections can err by

0.5–1 eV). The spurious effects (a) introduced from periodic images of the single defect include the following:

(i) The fact that the supercell is generally of order ~ 100 atoms or less and contains at least one defect implies a potentially unrealistically high concentration of carriers that would fill the conduction or valence band if the underlying defects have delocalized wave functions. This is the well-known Moss-Burstein band-filling effect for impurities in semiconductors. The band-filling *correction* works by replacing the interacting band dispersion due to shallow defect by an eigenstate at CBM (donor case) or VBM (acceptor case) [82,83].

(ii) The total energy formula for charged periodic system includes an arbitrary constant. To address this, the consistency between the defect system and the host system far away from the defect site requires aligning their electrostatic potential at a position in the defect cell that has minimal effects from the defect. The energy variation associated with this electrostatic potential shift ($q(V[D, q] - V[\text{host}])$) is the potential alignment correction.

(iii) The spurious interaction between charges in different supercells distorts the results due to finite size effects. The image charge correction [84] eliminates the spurious Coulomb interaction arising from such periodic image charges, for which we use the method of Lany and Zunger [52].

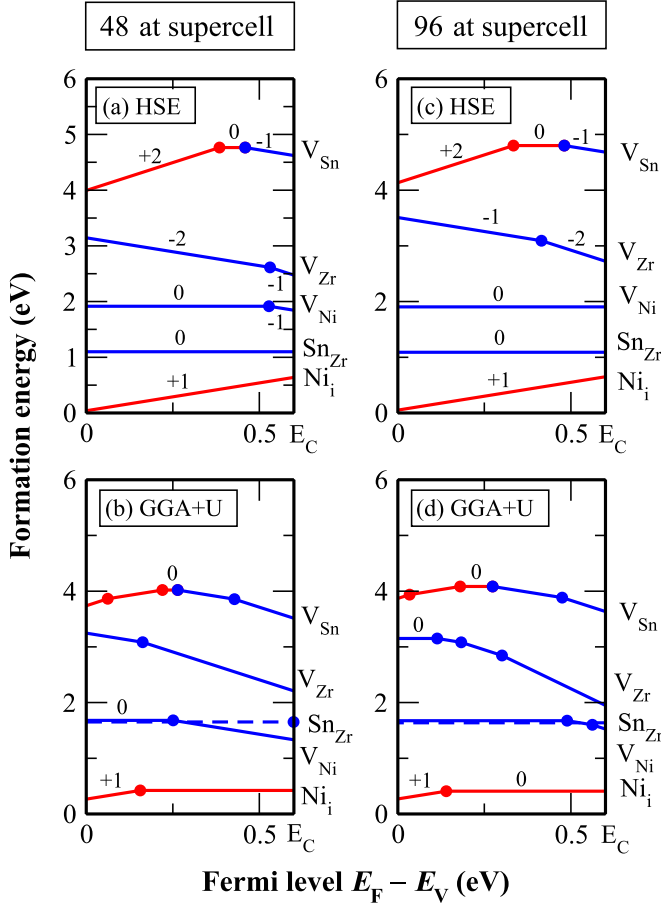


FIG. 15. Supercell size dependence of the HSE and GGA + U defect formation energies in ZrNiSn.

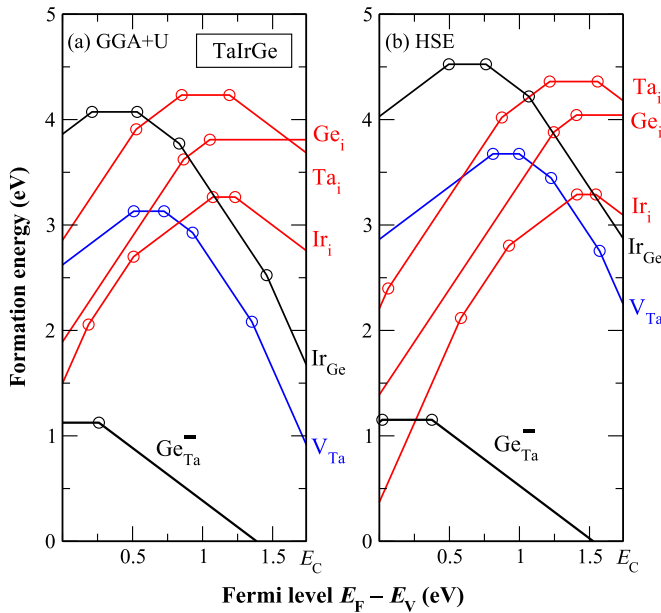


FIG. 16. Comparison between GGA + U and HSE study on formation energy of intrinsic defects in TaIrGe at the Ge-rich and Ta-poor condition in a 48-atom supercell. The computed equilibrium p -type carrier concentration is $1 \times 10^{17} \text{ cm}^{-3}$ in GGA + U and $5 \times 10^{16} \text{ cm}^{-3}$ by HSE.

TABLE II. Competing phases used for defining the chemical stability diagrams of ZrNiSn, ZrCoSb, ZrPtSn, ZrIrSb, and TaIrGe. A more thorough list of competing phases can be found in Table S2 in Ref. [14] for TaIrGe.

| ABX compound | ZrNiSn | ZrCoSb | ZrPtSn | ZrIrSb | TaIrGe |
|------------------|------------------------------------|---------------------------------|----------------------------------|-----------------------------------|---------------------------------|
| Competing phases | Zr ₃ Sn | ZrSb | Zr ₅ Sn ₃ | ZrSb | Ta ₃ Ge |
| | Zr ₅ Sn ₃ | ZrSb ₂ | Zr ₅ Sn ₄ | ZrSb ₂ | Ta ₅ Ge ₂ |
| | Zr ₅ Sn ₄ | Zr ₂ Sb | PtSn | Zr ₂ Sb | TaGe ₂ |
| | NiSn | Zr ₃ Sb | PtSn ₂ | Zr ₃ Sb | IrGe |
| | Ni ₃ Sn | Zr ₅ Sb ₃ | PtSn ₄ | Zr ₅ Sb ₃ | IrGe ₄ |
| | Ni ₃ Sn ₂ | Zr ₅ Sb ₄ | Pt ₂ Sn ₃ | Zr ₅ Sb ₄ | Ir ₄ Ge ₅ |
| | Ni ₃ Sn ₄ | CoSb | Pt ₃ Sn | IrSb | Ir ₃ Ge ₇ |
| | NiZr | CoSb ₂ | ZrPt | IrSb ₂ | TaIr |
| | Ni ₂ Zr | CoSb ₃ | ZrPt ₃ | IrSb ₃ | TaIr ₃ |
| | Ni ₃ Zr | ZrCo | Zr ₅ Pt ₃ | ZrIr | |
| | Ni ₅ Zr | ZrCo ₂ | Zr ₉ Pt ₁₁ | Zr ₂ Ir | |
| | ZrNi ₂ Sn | Zr ₂ Co | | ZrIr ₂ | |
| | ZrNi ₄ Sn | Zr ₃ Co | | ZrIr ₃ | |
| | Zr ₂ Ni ₂ Sn | | | Zr ₃ Ir | |
| | | | | Zr ₅ Ir ₃ | |
| | | | | Zr ₆ IrSb ₂ | |

The second class of corrections (b) pertains to the fact that irrespective of supercell size, DFT functionals, such as LDA or GGA, are known to introduce errors in band edges of the host compound and in the defect eigenstates. These entail specific postprocessor corrections described in Ref [52]. In the current paper, we use the hybrid functional (HSE) method [60,70,71] that performs rather well in terms of band gaps, so the class of corrections (b) is not needed in this case. Figure 15 describes the defect levels and defect formation energy in HSE, as well as uncorrected GGA + U in two supercell sizes. The conspicuous difference between HSE and GGA results lies in charge transition levels. For instance, ZrNiSn is the small band gap insulator ($E_g = 0.55 \text{ eV}$), posing difficulties for GGA to predict eigenvalues for in-gap states due to the lack of nonlocal exchange effect in GGA. The GGA functional wrongly predicted that Ni interstitial cannot ionize (Fig. 15); hence, the carrier density in ZrNiSn will be exceptional low ($\sim 10^{14} \text{ cm}^{-3}$), even if the total interstitial defect concentration is significant (10^{21} cm^{-3}), which contradicts the high n -type carrier density found in experiment. In the HSE study, the Ni_i is a shallow donor, ready to ionize and release carriers. Therefore, HSE is adopted in this defect study. The effect of increasing the supercell size from bcc-rhombohedral shape (48 atom) to simple cubic (96 atoms) on defect formation energy is rather minor (Fig. 15), since the separation between the nearest periodic images in the two cases are already large, 10.7 and 12.4 Å, respectively, and supercell correction is very helpful, although there exist small differences in transition levels of V_{Zr} and V_{Sn} from HSE calculations using the two supercells (Fig. 15).

c. Calculating compound formation enthalpies and chemical potentials

Regarding formation energies of compounds and the related chemical potentials, we calculated the excess chemical

TABLE III. Calculated formation enthalpies in units of electron volt per atom of five half-Heusler FTS (ZrNiSn, ZrCoSb, ZrPtSn, ZrIrSb, and TaIrGe) and their major competing phases.^a

| <i>(a) Five half-Heusler materials</i> | | | |
|--|----------------------------|---------------------------------|------------------------------|
| Half-Heusler materials | ΔH_f (eV/atom) DFT | ΔH_f (eV/atom) DFT+FERE | ΔH_f (eV/atom) Expt. |
| ZrNiSn | -0.656 | -0.943 | |
| ZrCoSb | -0.615 | -0.773 | |
| ZrPtSn | -1.032 | -1.153 | |
| ZrIrSb | -0.962 | -1.082 | |
| TaIrGe | -0.668 | -0.750 | |
| <i>(b) Competing phases for ZrNiSn</i> | | | |
| Compounds | ΔH_f (eV/atom) DFT | ΔH_f (eV/atom) DFT+FERE | ΔH_f (eV/atom) Expt. |
| Zr ₃ Sn | -0.289 | -0.850 | |
| Zr ₅ Sn ₃ | -0.552 | -1.026 | -0.738 |
| Zr ₅ Sn ₄ | -0.557 | -0.982 | |
| NiSn | -0.269 | -0.332 | |
| Ni ₃ Sn | -0.193 | -0.271 | -0.253 |
| Ni ₃ Sn ₂ | -0.284 | -0.353 | -0.301 |
| Ni ₃ Sn ₄ | -0.246 | -0.306 | -0.308 |
| NiZr* | -0.452 | | -0.523 |
| Ni ₂ Zr* | -0.410 | | |
| Ni ₃ Zr* | -0.463 | | |
| Ni ₅ Zr* | -0.326 | | |
| ZrNi ₂ Sn | -0.517 | -0.755 | |
| ZrNi ₄ Sn | -0.350 | -0.540 | |
| Zr ₂ Ni ₂ Sn | -0.564 | -0.902 | |
| <i>(c) Competing phases for ZrCoSb</i> | | | |
| Compounds | ΔH_f (eV/atom) DFT | ΔH_f (eV/atom) DFT+FERE | ΔH_f (eV/atom) Expt. |
| ZrSb | -0.695 | -0.977 | |
| ZrSb ₂ | -0.534 | -0.665 | -0.902 |
| Zr ₂ Sb | -0.589 | -1.022 | -1.043 |
| Zr ₃ Sb | -0.489 | -0.998 | -0.83 |
| Zr ₅ Sb ₃ | -0.617 | -1.012 | -1.116 |
| Zr ₅ Sb ₄ | -0.624 | -0.957 | |
| CoSb* | -0.164 | | -0.197 |
| CoSb ₂ * | -0.106 | | -0.176 |
| CoSb ₃ * | -0.142 | | -0.166 |
| ZrCo* | -0.291 | | -0.37 |
| ZrCo ₂ * | -0.311 | | -0.371 |
| Zr ₂ Co* | -0.254 | | -0.274 |
| Zr ₃ Co* | -0.200 | | |
| <i>(d) Competing phases for ZrPtSn</i> | | | |
| Compounds | ΔH_f (eV/atom) DFT | ΔH_f (eV/atom) DFT+FERE | ΔH_f (eV/atom) Expt. |
| Zr ₅ Sn ₃ | -0.552 | -1.026 | -0.738 |
| Zr ₅ Sn ₄ | -0.557 | -0.982 | |
| PtSn* | -0.646 | | -0.609 |
| PtSn ₂ * | -0.481 | | -0.542 |
| PtSn ₄ * | -0.295 | | -0.282 |
| Pt ₂ Sn ₃ * | -0.553 | | -0.564 |
| Pt ₃ Sn* | -0.469 | | -0.52 |
| ZrPt* | -1.084 | | -1.078 |
| ZrPt ₃ * | -1.017 | | |
| Zr ₅ Pt ₃ * | -0.813 | | |
| Zr ₉ Pt ₁₁ * | -0.784 | | |
| <i>(e) Competing phases for ZrIrSb</i> | | | |
| Compounds | ΔH_f (eV/atom) DFT | ΔH_f (eV/atom) DFT+FERE | ΔH_f (eV/atom) Expt. |
| ZrSb | -0.695 | -0.977 | |
| ZrSb ₂ | -0.534 | -0.665 | -0.902 |
| Zr ₂ Sb | -0.589 | -1.022 | -1.043 |
| Zr ₃ Sb | -0.489 | -0.998 | -0.83 |
| Zr ₅ Sb ₃ | -0.617 | -1.012 | -1.116 |

TABLE III. (Continued.)

| <i>(e) Competing phases for ZrIrSb</i> | | | |
|---|----------------------------|---------------------------------|------------------------------|
| Compounds | ΔH_f (eV/atom) DFT | ΔH_f (eV/atom) DFT+FERE | ΔH_f (eV/atom) Expt. |
| Zr ₅ Sb ₄ | -0.624 | -0.957 | |
| IrSb | -0.322 | -0.142 | -0.206 |
| IrSb ₂ | -0.438 | -0.261 | -0.151 |
| IrSb ₃ | -0.398 | -0.222 | -0.114 |
| ZrIr* | -0.770 | | -0.888 |
| Zr ₂ Ir* | -0.651 | | |
| ZrIr ₂ * | -0.674 | | |
| ZrIr ₃ * | -0.703 | | |
| Zr ₃ Ir* | -0.512 | | |
| Zr ₅ Ir ₃ * | -0.719 | | |
| Zr ₆ IrSb ₂ * | -1.115 | | |
| <i>(f) Competing phases for TaIrGe</i> | | | |
| Compounds | ΔH_f (eV/atom) DFT | ΔH_f (eV/atom) DFT+FERE | ΔH_f (eV/atom) Expt. |
| Ta ₃ Ge | -0.306 | -0.599 | |
| Ta ₅ Ge ₃ | -0.284 | -0.532 | |
| TaGe ₂ | -0.209 | -0.352 | |
| IrGe | -0.426 | -0.343 | |
| IrGe ₄ | -0.196 | -0.176 | |
| Ir ₄ Ge ₅ | -0.427 | -0.356 | |
| Ir ₃ Ge ₇ | -0.299 | -0.258 | |
| TaIr* | -0.587 | | |
| TaIr ₃ * | -0.682 | | |
| <i>(g) Summary of the FERE correction to GGA+U formation enthalpies when comparison with experimental data is available [74–76]</i> | | | |
| Compounds | ΔH_f (eV/atom) DFT | ΔH_f (eV/atom) DFT+FERE | ΔH_f (eV/atom) Expt. |
| Ni ₃ Sn | -0.193 | -0.271 | -0.253 |
| Ni ₃ Sn ₂ | -0.284 | -0.353 | -0.301 |
| Ni ₃ Sn ₄ | -0.246 | -0.306 | -0.308 |
| Zr ₅ Sn ₃ | -0.552 | -1.026 | -0.738 |
| ZrSb ₂ | -0.534 | -0.665 | -0.902 |
| Zr ₂ Sb | -0.589 | -1.022 | -1.043 |
| Zr ₃ Sb | -0.489 | -0.998 | -0.830 |
| Zr ₅ Sb ₃ | -0.617 | -1.012 | -1.116 |
| Zr ₅ Sn ₃ | -0.552 | -1.026 | -0.738 |
| IrSb | -0.322 | -0.142 | -0.206 |
| IrSb ₂ | -0.438 | -0.261 | -0.151 |
| IrSb ₃ | -0.398 | -0.222 | -0.114 |

^aThe DFT calculations were performed with the GGA + U method, except for those denoted by an asterisk (*) where plain GGA was used. The DFT+FERE method (see computational details in Sec. A.3) is applied only to the GGA + U results [73]. Calculations were compared to calorimetry data from Refs. [74–76].

potential diagrams using the formation enthalpies of each compound and its competing phases at the DFT – GGA + U level. Systematic DFT errors in formation energies of compounds were systematically corrected using the fitted elementary reference energy method (FERE [73]) in which the chemical potential of elemental phases (such as solid A or molecular C) obtained from GGA + U were shifted so that the calculated compound formation energies are fitted to the experimental data for a large set of binary and ternary compounds. The FERE-corrected GGA + U formation energy substantially improves the agreement with calorimetry data, especially for the Ni-Sn and Zr-Sb, Zr-Ir binary compounds (Table III; note that calorimetry data for ABC ternary compounds are rare.) For metal alloys and compounds, we use the plain GGA results rather than GGA + U , as the use of U is not well justified in such systems. Comparison with experiment on metal alloys is

also encouraging, e.g., in Pt-Sn and Zr-Co system, as well as for ZrIr and ZrPt (Table III). Further attempt using higher level functionals, such as HSE, was deemed unnecessary.

d. Atomic displacements and relaxation

To compute the local atomic displacements in each charge state, we start by introducing random displacements to the first nearest neighbor atoms around the defect site and assigned a magnetic moment of $0.7 \mu_B$ to the impurity atom to account for initial spin polarization. This step is needed to avoid locking of the displacement or magnetism at a local minima characterizing the ideal cubic structure. Then, all internal atomic positions are relaxed using the GGA + U method without any symmetry constraint until each component of the residual force was within $5 \times 10^{-3} \text{ eV/\AA}$. Using the fixed cell geometry obtained from GGA + U , we then evaluated the total

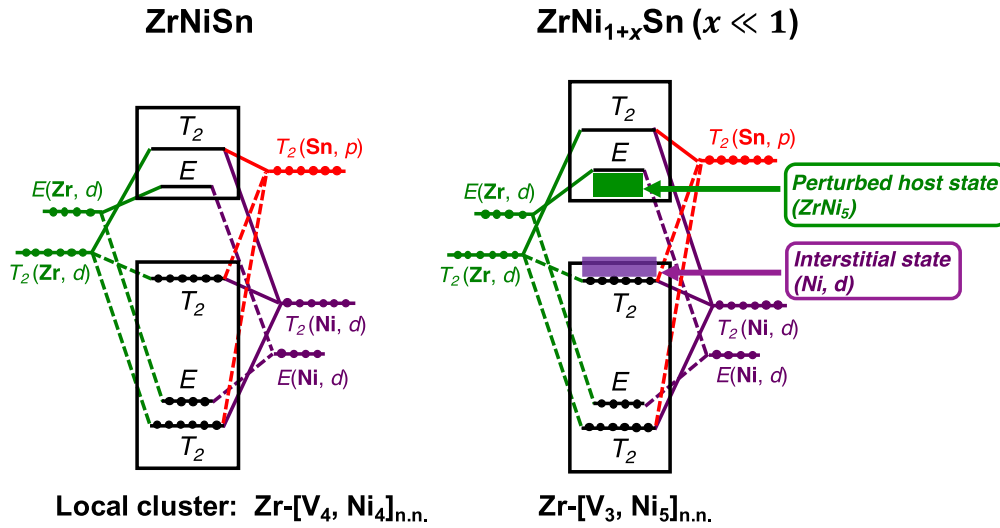


FIG. 17. Evolution of the orbital diagram from ZrNiSn to ZrNi_{1+x}Sn ($x \ll 1$), inducing the band gap reduction due to the formation of perturbed host state (PHS) (from a local ZrNi₅ cluster) near conduction band minimum (CBM) and the Ni interstitial states near the edge of the valence band maximum (VBM).

energy of the defect system by the hybrid functional method that included nonlocal exchange.

5. Stability and convergence of defect computational scheme

The adequacy of our defect computational scheme using a 48-atom BCC-type supercell is illustrated by a comparison to a 96-atom cubic supercell calculation in ZrNiSn (Fig. 15). Irrespective of the exchange-correlation functional (GGA+U or HSE approach), results on the defect formation energy and charge transition levels between the two supercell approaches tend to agree with each other, especially for defects with

low formation enthalpy. Defect results between GGA+U and HSE, however, show significant differences in charge transition levels, mainly due to the small band gap in ZrNiSn, which is challenging to defect level calculations in DFT. In TaIrGe (Fig. 16), there is a closer correspondence between GGA+U and HSE results for each charged defect, such that the computed equilibrium p -type carrier concentration agrees well among the two approaches— $1 \times 10^{17} \text{ cm}^{-3}$ by GGA+U versus $6 \times 10^{16} \text{ cm}^{-3}$ by HSE at room temperature from quench.

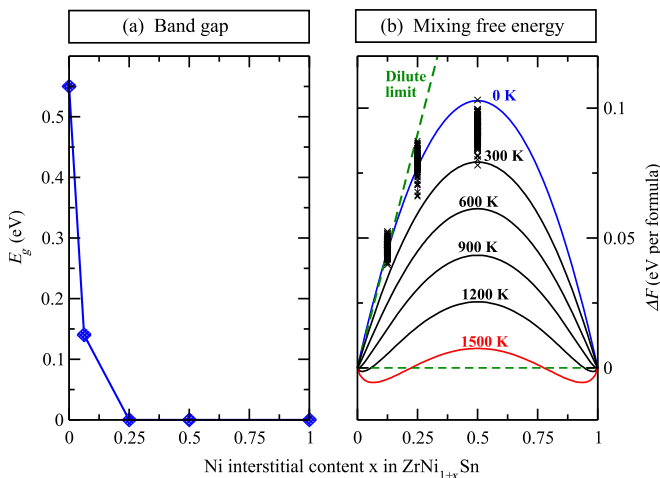


FIG. 18. Electronic band gap of ZrNi_{1+x}Sn from HSE study using a few configurations (a) and the temperature dependence of the mixing Helmholtz free energy versus Ni interstitial content x in ZrNi_{1+x}Sn, assuming a regular solid solution behavior: $\Delta F = wx(1-x) + k_B T(x \ln x + (1-x) \ln(1-x))$, with w being the Margules parameter for enthalpy of mixing, fitted to configurations within a $2 \times 2 \times 2$ supercell (b).

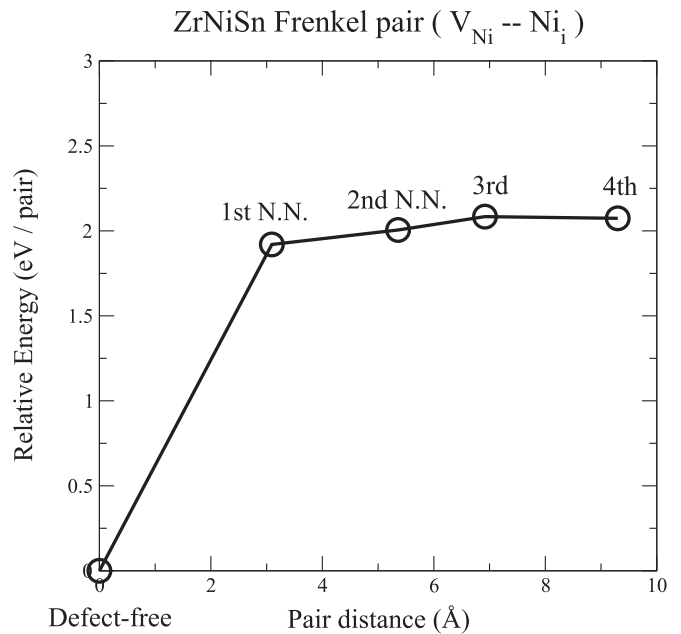


FIG. 19. Energetics of a Frenkel pair (Ni interstitial plus Ni vacancy) relative to the defect free host state as a function of the pair distance in a $2 \times 2 \times 2$ ZrNiSn supercell.

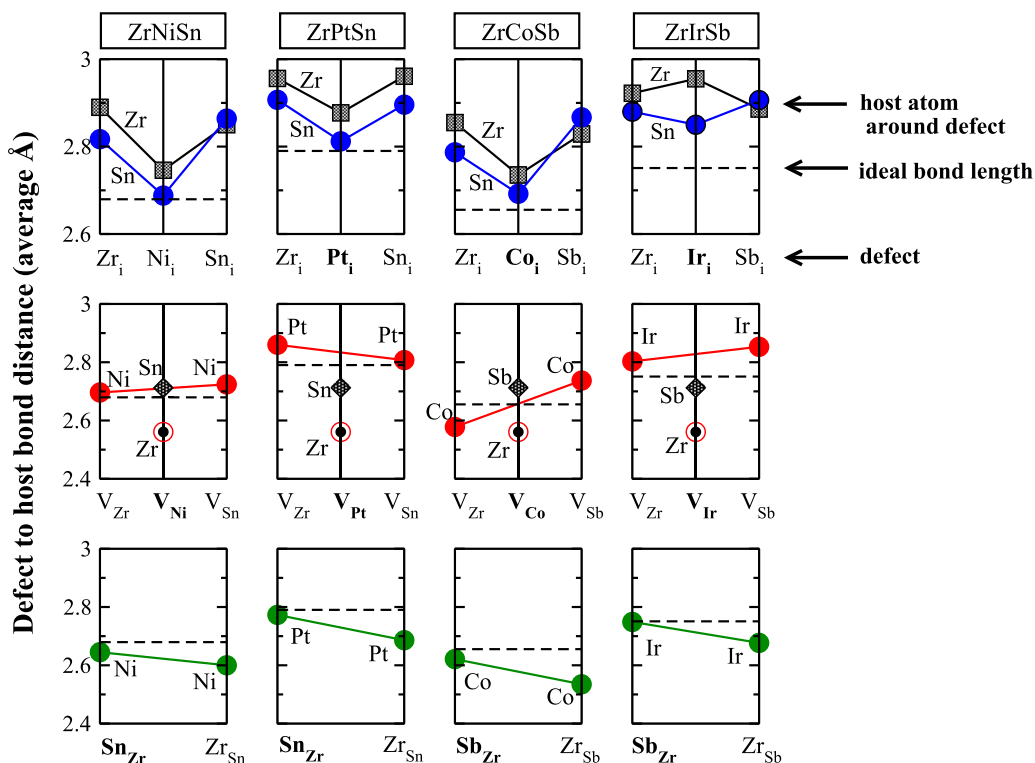


FIG. 20. The averaged first nearest neighbor bond distances from the defect centers to their surrounding host atoms—the bond lengths around the three interstitials: Zr_i , Ni_i , Sn_i (top row); three vacancies V_{Zr} , V_{Ni} , V_{Sn} (middle); and the two antisite defects, Sn_{Zr} and Zr_{Sn} (bottom).

6. $ZrNi_{1+x}Sn$: Band gaps and thermodynamics of mixing properties

Orbital diagram analysis in $ZrNiSn$ [Fig. 17(a)] shows that the lowest conduction band is an E state constituted mainly by the Zr d states while the VBM is formed by T_2 states, which are dominated by the Ni d states. The band gap reduction in $ZrNi_{1+x}Sn$ ($x \ll 1$) is due to the perturbed host state (from

a local $ZrNi_5$ cluster) near CBM and the Ni interstitial states near the edge of the VBM [Fig. 17(b)]. The HSE calculations with a few structure configurations in $ZrNi_{1+x}Sn$ show a sharp decrease in band gap with Ni interstitial addition, and the band gap plunges to zero at $x = 25\%$ [Fig. 18(a)]. Assuming a regular solution model between half-Heusler and full-Heusler alloy, we derived the Margules parameter for the enthalpy of mixing [$w = 0.4$ eV per formula in Fig. 18(b)], and find that at high temperature, e.g., 1500 K, there is a tendency to form intermediate compositions in the alloy—such as a Ni-poor

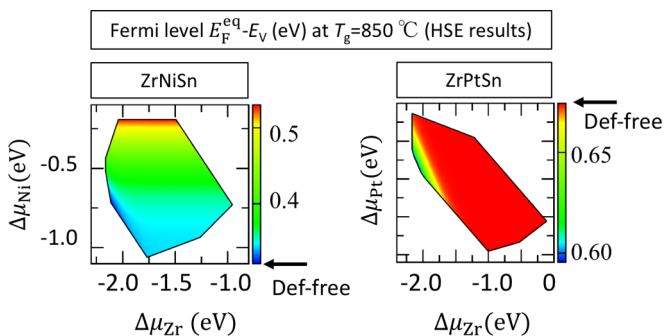


FIG. 21. The equilibrium Fermi level relative to the VBM at growth condition for the two ABC half-Heusler compounds due to self-doping mechanism arising from intrinsic defects: n -type $ZrNiSn$ and p -type $ZrPtSn$. It is the self-consistent solution to the charge neutrality condition [Eq. (A3)]. Please note that the Fermi level in defect (def)-free compounds are at $E_V + 0.33$ and $E_V + 0.67$ eV, respectively, for $ZrNiSn$ and $ZrPtSn$. The fundamental (Γ - X) band gaps of $ZrNiSn$ and $ZrPtSn$ are 0.55 and 1.28 eV, respectively (HSE results).

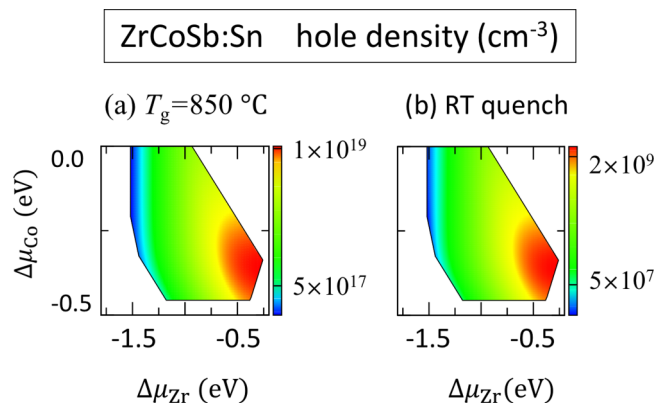


FIG. 22. The majority (hole) carrier density in Sn-doped $ZrCoSb$ as a function of excess chemical potential conditions at (a) growth condition ($T_g = 850$ °C) and (b) room temperature from quench after growth.

| | Donor | Acceptor |
|--------|--|---|
| ZrNiSn | Ni(i) Low ΔH V. shallow High n, T = 850 °C & RT Sb-doping: High n | V(Zr) High ΔH V. shallow Sn-on-Zr Low ΔH V. deep |
| ZrCoSb | Co(i) Low ΔH V. shallow High n, T = 850 °C & RT | V(Zr) Low ΔH deep Sn-on-Sb doping High p, T = 850 °C Low p, RT Sn-on-Sb Low ΔH deep |
| ZrPtSn | Pt(i) High ΔH V. deep Zr(i) High ΔH shallow | Sn-on-Zr Low ΔH deep High p, T = 850 °C Low p, RT V(Zr) High ΔH shallow |
| ZrIrSb | Sb-on-Zr Low ΔH deep Ir(i) High ΔH shallow | Sb-on-Zr Low ΔH deep High p, T = 850 °C Low p, RT V(Zr) High ΔH shallow |
| TaIrGe | Ir(i) High ΔH shallow Ge(i) High ΔH shallow | Ge-on-Ta Low ΔH shallow High p, T = 850 °C & RT V(Ta) High ΔH deep |

FIG. 23. Summary of doping trends in five *ABC* compounds (ZrNiSn, ZrCoSb, ZrPtSn, ZrIrSb, and TaIrGe). For each system, we show the dominant donors (red frame) and dominant acceptors (blue frame), indicating for each defect if its formation energy at equilibrium Fermi level is “high,” as well as if the transition level is shallow (i.e., carrier producing) or deep (i.e., carriers are not released). Dominant (high density) defects are shown in bold face. We used the following notation: “V. shallow” stands for “very shallow”; “high n” and “high p” denote “high *n*-type density” and “high *p*-type density,” respectively.

phase in the half-Heusler end, ZrNi_{1.07}Sn, and a Ni-rich phase in the Heusler end, ZrNi_{1.93}Sn [Fig. 18(b)].

7. Frenkel defects in ZrNiSn

The energy required to create a single Frankel defect in ZrNiSn is rather high (~2 eV) and barely changes with the distance between the Ni interstitial and Ni vacancy separation (Fig. 19). Hence it is unfavorable to form Frenkel defects in ZrNiSn.

8. Bond lengths around dominant single defects in four half-Heusler compounds

To one’s surprise, we find a nearly exact match between ideal bond lengths and the relaxed bond lengths for *B* interstitial and *C*-on-*A* antisite defects in the four selected compounds (ZrNiSn, ZrPtSn, ZrCoSb, ZrIrSb), as shown in Fig. 20 with an exception case being Ir_i. On the other hand, both *A*

interstitials and *C* interstitials produce significant bond length expansion, indicating they are energetically unfavorable. This is well consistent with the rule of conservation of coordination number and the symmetry analysis in Sec. III D.

9. Equilibrium Fermi level, carrier density, and charged defect concentration versus chemical potential conditions

The self-consistent solution to the charge neutrality condition in carrier doping study [Eq. (A3)] depends strongly on chemical potential conditions. For example, in ZrNiSn (Fig. 21), at the most Ni-poor condition the equilibrium Fermi level (E_F^{eq}) is pinned to the middle of the band gap (~ $E_V + 0.3$ eV). Accidentally this Fermi level position can also be achieved if the ZrNiSn sample were defect-free. In contrast, at the most Ni-rich condition, E_F^{eq} is pinned close to CBM due to the ionization of Ni interstitials. In ZrPtSn (Fig. 21), E_F^{eq} is pinned to the middle of the gap (~ $E_V + 0.67$ eV) at defect-free conditions, but at the *C*-rich-*A* poor condition (the lower left region in the stability field), the presence of the antisite

(Sn-on-Zr)²⁻ acceptors pins E_F^{eq} closer to VBM ($\sim E_V + 0.6$ eV), thus introducing holes into the host. In Fig. 22, the hole carrier density in Sn-doped ZrCoSb shows maximum at the Co-poor and Sb-poor condition (the lower right corner in the stability field), because the Co-poor condition suppresses Co-interstitial donors which kill holes, while Sb-poor condition is beneficial to the creation of Sn-on-Sb substitution. An example for the variation of charged impurity concentration as a function of chemical potential condition is discussed in Fig. 11, which is analogous to the total impurity concentration diagram in Fig. 4.

10. Doping trends in five ABC compounds

We summarize in Fig. 23 our defect computational results for the dominant donors and acceptors in ZrNiSn, ZrCoSb, ZrPtSn, ZrIrSb, and TaIrGe. The characteristics of the dominant donors (or acceptors) and their primary opponents are described in terms of defect formation energy, transition levels, and resulting equilibrium carriers, which serves as the key doping information for the five compounds. The formation energy and carrier density are described at the equilibrium Fermi level condition.

-
- [1] E. Parthe, *Crystal Chemistry of Tetrahedral Structures* (Gordon and Breach Science Publishers, New York, 1964).
- [2] L. I. Berger, *Semiconductor Materials* (CRC Press, Boca Raton, FL, 1996).
- [3] H. Nowotny and W. Siebert, *Zeit. Met.* **33**, 391 (1941).
- [4] H. Nowotny and K. Bachmayer, *Monatshefte Chem. Verwandte Teile And. Wiss.* **81**, 488 (1950).
- [5] R. Juza and F. Hund, *Z. Anorg. Chem.* **257**, 1 (1948).
- [6] R. Juza and F. Hund, *Naturwissenschaften* **33**, 121 (1946).
- [7] D. M. Wood, A. Zunger, and R. de Groot, *Phys. Rev. B* **31**, 2570 (1985).
- [8] A. E. Carlsson, A. Zunger, and D. M. Wood, *Phys. Rev. B* **32**, 1386 (1985).
- [9] S.-H. Wei and A. Zunger, *Phys. Rev. Lett.* **56**, 528 (1986).
- [10] F. Casper, T. Graf, S. Chadov, B. Balke, and C. Felser, *Semicond. Sci. Technol.* **27**, 063001 (2012).
- [11] F. Casper, R. Seshadri, and C. Felser, *Phys. Status Solidi A* **206**, 1090 (2009).
- [12] X. W. Zhang, L. P. Yu, A. Zakutayev, and A. Zunger, *Adv. Funct. Mater.* **22**, 1425 (2012).
- [13] R. Gautier, X. W. Zhang, L. H. Hu, L. P. Yu, Y. Y. Lin, T. O. L. Sunde, D. Chon, K. R. Poeppelmeier, and A. Zunger, *Nat. Chem.* **7**, 308 (2015).
- [14] F. Yan, X. W. Zhang, Y. G. Yu, L. P. Yu, A. Nagaraja, T. O. Mason, and A. Zunger, *Nat. Commun.* **6**, 7308 (2015).
- [15] *ICSD, Inorganic Crystal Structure Database* (Fachinformationzentrum Karlsruhe, Karlsruhe, Germany, 2013).
- [16] S. Chadov, X. Qi, J. Kubler, G. H. Fecher, C. Felser, and S. C. Zhang, *Nat. Mater.* **9**, 541 (2010).
- [17] H. Lin, L. A. Wray, Y. Xia, S. Xu, S. Jia, R. J. Cava, A. Bansil, and M. Z. Hasan, *Nat. Mater.* **9**, 546 (2010).
- [18] A. Roy, J. W. Bennett, K. M. Rabe, and D. Vanderbilt, *Phys. Rev. Lett.* **109**, 037602 (2012).
- [19] S. Wang, Z. Wang, W. Setyawan, N. Mingo, and S. Curtarolo, *Phys. Rev. X* **1**, 021012 (2011).
- [20] G. J. Snyder and E. S. Toberer, *Nat. Mater.* **7**, 105 (2008).
- [21] G. J. Snyder and T. S. Ursell, *Phys. Rev. Lett.* **91**, 148301 (2003).
- [22] C. Uher, J. Yang, S. Hu, D. T. Morelli, and G. P. Meisner, *Phys. Rev. B* **59**, 8615 (1999).
- [23] K. Ishizaka, M. S. Bahramy, H. Murakawa, M. Sakano, T. Shimojima, T. Sonobe, K. Koizumi, S. Shin, H. Miyahara, A. Kimura, K. Miyamoto, T. Okuda, H. Namatame, M. Taniguchi, R. Arita, N. Nagaosa, K. Kobayashi, Y. Murakami, R. Kumai *et al.*, *Nat. Mater.* **10**, 521 (2011).
- [24] J. Kübler, A. R. William, and C. B. Sommers, *Phys. Rev. B* **28**, 1745 (1983).
- [25] R. A. de Groot, F. M. Mueller, P. G. van Engen, and K. H. J. Buschow, *Phys. Rev. Lett.* **50**, 2024 (1983).
- [26] N. P. Butch, P. Syers, K. Kirshenbaum, A. P. Hope, and J. Paglione, *Phys. Rev. B* **84**, 220504 (2011).
- [27] W. Al-Sawai, H. Lin, R. S. Markiewicz, L. A. Wray, Y. Xia, S. Y. Xu, M. Z. Hasan, and A. Bansil, *Phys. Rev. B* **82**, 125208 (2010).
- [28] G. Trimarchi, X. Zhang, M. J. DeVries Vermeer, J. Cantwell, K. R. Poeppelmeier, and A. Zunger, *Phys. Rev. B* **92**, 165103 (2015).
- [29] M. J. D. Vermeer, X. Zhang, G. Trimarchi, M. D. Donakowski, P. J. Chupas, K. R. Poeppelmeier, and A. Zunger, *J. Am. Chem. Soc.* **137**, 11383 (2015).
- [30] A. Zakutayev, X. Zhang, A. Nagaraja, L. Yu, S. Lany, T. O. Mason, D. S. Ginley, and A. Zunger, *J. Am. Chem. Soc.* **135**, 10048 (2013).
- [31] S. V. Dudiy and A. Zunger, *Phys. Rev. Lett.* **97**, 046401 (2006).
- [32] A. Franceschetti, S. V. Dudiy, S. V. Barabash, A. Zunger, J. Xu, and M. van Schilfgaarde, *Phys. Rev. Lett.* **97**, 047202 (2006).
- [33] A. Franceschetti and A. Zunger, *Nature (London)* **402**, 60 (1999).
- [34] Y. Xia, V. Ponnambalam, S. Bhattacharya, A. L. Pope, S. J. Poon, and T. M. Tritt, *J. Phys.: Condens. Matter* **13**, 77 (2001).
- [35] J. P. Heremans, V. Jovovic, E. S. Toberer, A. Saramat, K. Kurosaki, A. Charoenphakdee, S. Yamanaka, and G. J. Snyder, *Science* **321**, 554 (2008).
- [36] R. S. M. Wambach, S. Bhattacharya, P. Ziolkowski, E. Müller, G. K. H. Madsen, and A. Ludwig, *Adv. Electron. Mater.* **2**, 1500208 (2016).
- [37] J. E. Douglas, C. S. Birkel, M.-S. Miao, C. J. Torbet, G. D. Stucky, T. M. Pollock, and R. Seshadri, *Appl. Phys. Lett.* **101**, 183902 (2012).
- [38] J. K. Kawasaki, L. I. M. Johansson, B. D. Schultz, and C. J. Palmstrøm, *Appl. Phys. Lett.* **104**, 022109 (2014).
- [39] Y. Pei, A. F. May, and G. J. Snyder, *Adv. Energy Mater.* **1**, 291 (2011).
- [40] Y. V. Stadnyk, V. A. Romaka, Y. K. Gorelenko, L. P. Romaka, D. Fruchart, and V. F. Chekurin, *J. Alloys Comp.* **400**, 29 (2005).
- [41] H. Hohl, A. P. Ramirez, C. Goldmann, G. Ernst, B. Wölfing, and E. Bucher, *J. Phys.: Condens. Matter* **11**, 1697 (1999).
- [42] T. Wu, W. Jiang, X. Li, Y. Zhou, and L. Chen, *J. Appl. Phys.* **102**, 103705 (2007).

- [43] H. Xie, H. Wang, C. Fu, Y. Liu, G. J. Snyder, X. Zhao, and T. Zhu, *Sci. Rep.* **4**, 6888 (2014).
- [44] V. V. Romaka, P. Rogl, L. Romaka, Y. Stadnyk, A. Grytsiv, O. Lakh, and V. Krayovskii, *Intermetallics* **35**, 45 (2013).
- [45] A. Zunger, *Appl. Phys. Lett.* **83**, 57 (2003).
- [46] J. P. Perdew and A. Zunger, *Phys. Rev. B* **23**, 5048 (1981).
- [47] J. Schmitt, Z. M. Gibbs, G. J. Snyder, and C. Felser, *Mater. Horiz.* **2**, 68 (2015).
- [48] F. G. Aliev, N. B. Brandt, V. V. Kozyrkov, V. V. Moshchalkov, R. V. Skolozdra, Y. V. Stadnyk, and V. K. Pecharskii, *JETP Lett.* **45**, 684 (1987).
- [49] S. Ögüt and K. M. Rabe, *Phys. Rev. B* **51**, 10443 (1995).
- [50] K. Miyamoto, A. Kimura, K. Sakamoto, M. Ye, Y. Cui, K. Shimada, H. Namatame, M. Taniguchi, S. Fujimori, Y. Saitoh, E. Ikenaga, K. Kobayashi, J. Tadano, and T. Kanomata, *Appl. Phys. Lett.* **96**, 152105 (2010).
- [51] P. Larson, S. D. Mahanti, and M. G. Kanatzidis, *Phys. Rev. B* **62**, 12754 (2000).
- [52] S. Lany and A. Zunger, *Phys. Rev. B* **78**, 235104 (2008).
- [53] P. R. C. Kent and A. Zunger, *Phys. Rev. Lett.* **86**, 2613 (2001).
- [54] D. T. Do, S. D. Mahanti, and J. J. Pulikkoti, *J. Phys.: Condens. Matter* **26**, 275501 (2014).
- [55] K. Miyamoto *et al.*, *Appl. Phys. Express* **1**, 081901 (2008).
- [56] V. A. Romaka, P. Rogl, V. V. Romaka, Y. V. Stadnyk, E. K. Hlil, V. Y. Krajevskii, and A. M. Horyn, *Semiconductors* **47**, 892 (2013).
- [57] R. Shan, E. V. Vilanova, J. Qin, F. Casper, G. H. Fecher, G. Jakob, and C. Felser, *Phys. Status Solidi RRL* **7**, 145 (2013).
- [58] K. Mastronardi, D. Young, C.-C. Wang, P. Khalifah, R. J. Cava, and A. P. Ramirez, *Appl. Phys. Lett.* **74**, 1415 (1999).
- [59] T. Sekimoto, K. Kurosaki, H. Muta, and S. Yamanaka, *Mater. Trans.* **48**, 2079 (2007).
- [60] J. Heyd, G. E. Scuseria, and M. Ernzerhof, *J. Chem. Phys.* **118**, 8207 (2003).
- [61] J. Buckeridge, D. O. Scanlon, A. Walsh, and C. R. A. Catlow, *Comput. Phys. Commun.* **185**, 330 (2014).
- [62] K. Irmscher, M. Naumann, M. Pietsch, Z. Galazka, R. Uecker, T. Schulz, R. Schewski, M. Albrecht, and R. Fornari, *Phys. Status Solidi A* **211**, 54 (2014).
- [63] F. J. Manjón, M. Mollar, M. A. Hernández-Fenollosa, B. Marí, R. Lauck, and M. Cardona, *Solid State Commun.* **128**, 35 (2003).
- [64] J. D. Perkins, T. R. Paudel, A. Zakutayev, P. F. Ndione, P. A. Parilla, D. L. Young, S. Lany, D. S. Ginley, A. Zunger, N. H. Perry, Y. Tang, M. Grayson, T. O. Mason, J. S. Bettinger, Y. Shi, and M. F. Toney, *Phys. Rev. B* **84**, 205207 (2011).
- [65] S. Bhattacharya, A. L. Pope, R. T. Littleton, T. M. Tritt, V. Ponnambalam, Y. Xia, and S. J. Poon, *Appl. Phys. Lett.* **77**, 2476 (2000).
- [66] J. E. Douglas, C. S. Birkel, N. Verma, V. M. Miller, M.-S. Miao, G. D. Stucky, T. M. Pollock, and R. Seshadri, *J. Appl. Phys.* **115**, 043720 (2014).
- [67] J. Osorio-Guillén, S. Lany, S. V. Barabash, and A. Zunger, *Phys. Rev. B* **75**, 184421 (2007).
- [68] P. Qiu, X. Huang, X. Chen, and L. Chen, *J. Appl. Phys.* **106**, 103703 (2009).
- [69] Y. Kimura, A. Zama, and Y. Mishima, in *Proceedings of the 2006 25th International Conference on Thermoelectrics (IEEE, Piscataway, NJ, 2006)*, pp. 115–119.
- [70] J. Heyd, G. E. Scuseria, and M. Ernzerhof, *J. Chem. Phys.* **124**, 219906 (2006).
- [71] J. Heyd and G. E. Scuseria, *J. Chem. Phys.* **121**, 1187 (2004).
- [72] Y. W. Chai and Y. Kimura, *Acta Mater.* **61**, 6684 (2013).
- [73] V. Stevanović, S. Lany, X. W. Zhang, and A. Zunger, *Phys. Rev. B* **85**, 115104 (2012).
- [74] W. E. Liu and S. E. Mohny, *Mater. Sci. Eng., B* **103**, 189 (2003).
- [75] S. V. Meschel and O. J. Kleppa, *Thermochim. Acta* **314**, 205 (1998).
- [76] L. Topor and O. J. Kleppa, *Metall. Trans. A* **19**, 1827 (1988).
- [77] L. Stephan and Z. Alex, *Modell. Simul. Mater. Sci. Eng.* **17**, 084002 (2009).
- [78] C. Freysoldt, B. Grabowski, T. Hickel, J. Neugebauer, G. Kresse, A. Janotti, and C. G. Van de Walle, *Rev. Mod. Phys.* **86**, 253 (2014).
- [79] J. Ihm, A. Zunger, and M. L. Cohen, *J. Phys. C* **12**, 4409 (1979).
- [80] G. Kresse and J. Hafner, *Phys. Rev. B* **47**, 558 (1993).
- [81] G. Kresse and J. Furthmüller, *Comput. Mater. Sci.* **6**, 15 (1996).
- [82] T. S. Moss, *Proc. Phys. Soc. London, Sect. B* **67**, 775 (1954).
- [83] E. Burstein, *Phys. Rev.* **93**, 632 (1954).
- [84] G. Makov and M. C. Payne, *Phys. Rev. B* **51**, 4014 (1995).